A small periplasmic protein governs broad physiological adaptations in *Vibrio cholerae* via regulation of the DbfRS two-component system

Emmy Nguyen[1], Charles Agbavor[2], Anjali Steenhaut[3], M R Pratyush[1], N. Luisa Hiller[1], Laty A. Cahoon[2], Irina V. Mikheyeva[1], Wai-Leung Ng[3], Andrew A. Bridges[1,*]

[1]Department of Biological Sciences, Carnegie Mellon University, Pittsburgh, PA 15213, USA

[2]Department of Biological Sciences, University of Pittsburgh, Pittsburgh, PA 15260, USA

[3]Department of Molecular Biology and Microbiology, Tufts University School of Medicine, Boston, MA 02111, USA

*Correspondence to Andrew. A Bridges: bridges@cmu.edu

Abstract

Two-component signaling pathways allow bacteria to sense and respond to environmental changes, yet the sensory mechanisms of many remain poorly understood. In the pathogen *Vibrio cholerae*, the DbfRS two-component system controls the biofilm lifecycle, a critical process for environmental persistence and host colonization. Here, we identified DbfQ, a small periplasmic protein encoded adjacent to *dbfRS*, as a direct modulator of pathway activity. DbfQ directly binds the sensory domain of the histidine kinase DbfS, shifting it toward phosphatase activity and promoting biofilm dispersal. In contrast, outer membrane perturbations, caused by mutations in lipopolysaccharide biosynthesis genes or membrane-damaging antimicrobials, activate phosphorylation of the response regulator DbfR. Transcriptomic analyses reveal that DbfR phosphorylation leads to broad transcriptional changes spanning genes involved in biofilm formation, central metabolism, peptidoglycan synthesis, and cellular stress responses. Constitutive DbfR phosphorylation imposes severe fitness costs in an infection model, highlighting this pathway as a potential target for anti-infective therapeutics. We find that *dbfQRS*-like genetic modules are widely present across bacterial phyla, underscoring their broad relevance in bacterial physiology. Collectively, these findings establish DbfQ as a new class of periplasmic regulator that influences two-component signaling and bacterial adaptation.

Introduction

Microorganisms must adapt to environmental fluctuations to ensure their persistence. As a result, over evolution, bacteria have developed sophisticated sensory mechanisms that translate environmental signals into adaptive responses. Among these mechanisms, two-component systems (TCSs), which consist of a membrane-associated sensor histidine kinase and a cognate response regulator, are ubiquitous across the bacterial domain (1, 2). Upon the detection of specific stimuli, histidine kinases modify the phosphorylation state of the response regulator which, in turn, orchestrates physiological changes, often through regulation of gene expression (3–5). The prevalence and diversity of TCSs in bacterial genomes is immense, with some individual species encoding as many as 200 distinct TCSs (6). Despite their pervasiveness, research into TCS molecular mechanisms has primarily concentrated on a handful of major TCS families (7–9). As a result, for most TCSs, the identities of their stimuli, mechanisms of signal transduction, and consequences to bacterial physiology remain underexplored.

TCSs frequently control bacterial social behaviors, including regulation of the biofilm lifecycle, whereby bacteria form surface-associated, multicellular communities (10–13). In the biofilm state, bacterial cells are encased in a self-produced extracellular matrix that confers environmental protection against antimicrobials, immune responses, fluid flow, and bacteriophage predation (14–17). For these reasons, biofilms are notoriously difficult to eradicate in both clinical and industrial settings. Despite the adaptive benefits of the biofilm lifestyle, prolonged biofilm formation can be associated with bacterial fitness costs. Dense multicellular communities face competition for resources, their surface-associated characteristic limits spread to new territories, and extracellular matrix production diverts resources from metabolic processes (18–20). Consequently, bacteria have evolved intricate sensory mechanisms, often involving TCSs, to control the balance of biofilm formation and biofilm dispersal, whereby cells transition to the free-swimming state (21–23).

For *Vibrio cholerae*, the causative agent of cholera disease, the biofilm lifecycle is thought to underlie its ability to transition between the aquatic niche and the human host (24–26). Moreover, transitions between bacterial niches are often mediated by TCSs, enabling host adaptation in facultative pathogens such as *V. cholerae* (27–29). In prior work, we identified a TCS, named DbfRS (encoded by *vc_1638* and *vc_1639*), as a regulator of *V. cholerae* biofilm lifecycle transitions (30). Within this cascade, DbfS serves as the sensor histidine kinase that controls the phosphorylation state of the transcription factor DbfR (Fig. 1A). The balance between kinase and phosphatase activities of DbfS determines the phosphorylation state of DbfR, which in turn dictates whether cells commit to the biofilm state or disperse. Specifically, dephosphorylation of DbfR enables biofilm dispersal, whereas DbfR phosphorylation activates biofilm formation and represses dispersal via positive regulation of biofilm matrix gene expression (Fig. 1A). Beyond these

basic findings, the DbfRS pathway remains uncharacterized - the environmental signal(s) controlling pathway activity remain unknown, the DbfR regulon is undefined, and its role during infection is unclear.

In this study, we comprehensively investigated the DbfRS regulatory network, defining its sensory inputs, physiological outputs, and fitness consequences. We identified a previously uncharacterized small protein, DbfQ, that directly interacts with and modulates the sensory domain of DbfS, driving the receptor toward phosphatase activity. We find that outer membrane stresses activate the DbfQRS pathway and that DbfR phosphorylation leads to global transcriptional changes, coordinating biofilm commitment and peptidoglycan maintenance with reduced metabolic activity. Activation of the DbfQRS pathway is detrimental to bacterial colonization in an animal model of infection, highlighting the potential of this pathway as a therapeutic target for limiting the spread of *V. cholerae*. Finally, the widespread occurrence of *dbfQRS*-like genetic modules, including in other important pathogens, underscores the broader relevance of this novel regulatory mechanism.

Results

A small protein controls the biofilm lifecycle via regulation of the DbfRS signaling cascade

For many bacterial TCSs, the genes encoding response regulator and histidine kinase pairs commonly exist within the same operon. Examination of the *dbfRS* operon revealed a third gene, herein referred to as *dbfQ*, encoded immediately upstream and predicted to be co-transcribed with *dbfRS* (Fig. 1B) (31). Given its presumed co-regulation, we wondered whether DbfQ could participate in regulating the biofilm lifecycle via the DbfRS signaling pathway. *dbfQ* encodes a 135-amino-acid protein with a predicted N-terminal secretion signal (Sec/SPI) (32). The predicted mature ~12kDa protein harbors a single Pfam domain, annotated as PepSY (residues 74 to 122) (33). Several studies have implicated PepSY domains in metal binding and/or protease inhibition (34, 35), though the exact role of this motif is unclear. To determine whether DbfQ modulates the biofilm lifecycle, we constructed an in-frame deletion of *dbfQ*. Similar to the Δ*dbfS* mutant, the Δ*dbfQ* strain exhibited enhanced biofilm formation and a defect in biofilm dispersal, with substantial biofilm biomass remaining at the final timepoint (Fig. 1C). Both mutants also exhibited a growth defect compared to wild-type (WT) (Fig. S1A). Complementation of the Δ*dbfQ* mutant by introducing P_{tac}-*dbfQ* at a neutral locus restored the biofilm lifecycle and growth rate to that of WT (Fig. S1B-E). To determine whether DbfQ controls the biofilm lifecycle via the DbfRS cascade, we introduced the Δ*dbfQ* deletion into a strain harboring a non-phosphorylatable allele of *dbfR* (*dbfR*^{D51V}), rendering it unresponsive to DbfS activity. We found that the Δ*dbfQ dbfR*^{D51V} double mutant did not exhibit the altered biofilm phenotype measured for the Δ*dbfQ* mutant (Fig. 1D), supporting a model in which

DbfQ regulates biofilm dynamics through the DbfRS signaling pathway, presumably by modulating DbfS activity.

Bacterial TCSs show a broad range of conservation, with some TCSs exhibiting a high degree of similarity across diverse taxa, whereas others are present only in specific lineages (36). Given this understanding, we wondered whether DbfQ-like proteins encoded adjacent to TCSs are widespread. To investigate the pervasiveness of the DbfQRS module, we conducted a bioinformatic search for gene neighborhoods in which a small PepSY domain-containing protein was encoded in the vicinity of a histidine kinase or response regulator (vicinity was defined as within four genes). We found that such gene neighborhoods were present across multiple bacterial phyla, with a large representation of Proteobacteria as well as instances in Terrabacteria and Fusobacteria (Fig. 1E, Fig. S2). Indeed, the observed frequency of a PepSY-domain protein encoded in proximity to a TCS was >60-fold higher than expected by chance (see Methods). Notably, DbfQRS-like modules are present in numerous bacteria associated with human infections and agriculture (Fig. 1E). The organization of these genetic modules varied with, in some cases, two DbfQ-like proteins encoded upstream of the TCS (e.g. *Pseudomonas aeruginosa*) (Fig. 1E). In other cases, PepSY-protein and TCS genes were adjacent but encoded on opposite strands (e.g. *Burkholderia pseudomallei*) (Fig. 1E). Collectively, these findings show that DbfQRS-like genetic modules are widespread, suggestive of a potentially conserved regulatory principle at play across diverse bacteria.

Given the dramatic effect of DbfQ on the biofilm lifecycle of *V. cholerae*, combined with the widespread presence of DbfQRS modules, we sought to determine the molecular mechanisms by which DbfQ impinges upon the TCS. Prior work demonstrated that DbfS functions as a phosphatase under laboratory growth conditions, permitting biofilm dispersal (30). In the Δ*dbfS* mutant, DbfR is phosphorylated by an unidentified kinase or small molecule phosphate donor, leading to increased biofilm formation and inhibited dispersal. We set out to confirm this relationship using Phos-tag gel analysis, where more negatively charged, phosphorylated species migrate slower than the dephosphorylated form. Consistent with earlier findings, in the absence of *dbfS*, a distinct second, slower-migrating band corresponding to phosphorylated DbfR was detected (Fig. 1F). As histidine kinases typically switch between kinase and phosphatase modes depending on the ligand occupancy of their sensory domains, we reasoned that DbfQ could influence the balance between these catalytic activities of DbfS. To test this possibility, we examined DbfR phosphorylation in the Δ*dbfQ* mutant strain and observed complete phosphorylation of the DbfR response regulator (Fig. 1F). In contrast, the Δ*dbfQ* Δ*dbfS* double mutant phenocopied the Δ*dbfS* single mutant, demonstrating that DbfQ controls DbfR phosphorylation, and in turn the biofilm lifecycle, by modulating the kinase-phosphatase equilibrium of DbfS. Because DbfR is phosphorylated in the absence of DbfQ, our results suggest that DbfQ biases DbfS towards phosphatase activity. Together, these results

demonstrate that DbfQ acts as a key regulator of the DbfRS signaling cascade, impinging on the biofilm lifecycle by controlling the activity of the DbfS receptor.

To establish a quantitative readout of DbfQRS signal transduction, we set out to generate a luminescent reporter for pathway activity. During Phos-tag analysis (Fig. 1F), we noticed that increased DbfR phosphorylation appeared to correlate with elevated DbfR levels, suggestive of positive autoregulation of the *dbfQRS* operon, a common feature of bacterial TCSs (3). Thus, to generate a luminescent reporter for DbfR phosphorylation, we fused the *dbfQRS* promoter to luciferase (P_{dbfQRS}-*lux*). To validate the reporter, we first measured luminescence in the Δ*dbfS and* Δ*dbfQ* mutants which, as shown above, exhibit elevated DbfR phosphorylation (Fig. 1F). Both mutants displayed a ~40-fold increase in luminescence compared to the WT strain (Fig. 1G). Moreover, introduction of the phospho-dead $dbfR^{D51V}$ allele into the Δ*dbfS and* Δ*dbfQ* mutant backgrounds reduced light production to below that of WT, demonstrating that P_{dbfQRS}-*lux* reports on DbfR phosphorylation state.

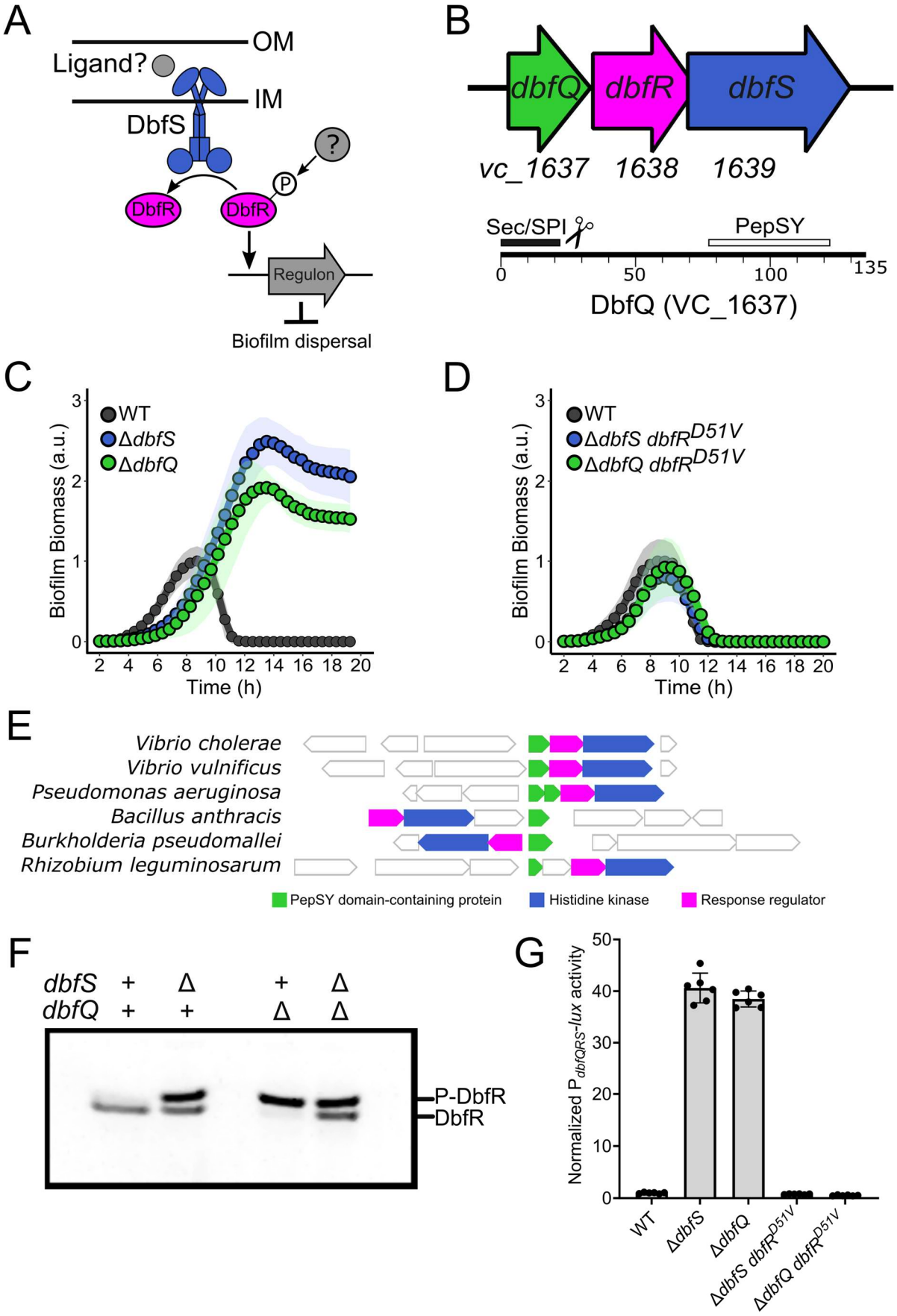

Figure 1. DbfQ regulates the biofilm lifecycle via modulation of the DbfRS signaling cascade. (A) Initial model for DbfRS regulation of the biofilm lifecycle. OM = outer membrane, IM = inner membrane. Grey objects remain uncharacterized. (B) Top panel: Operon structure of the genes encoding the DbfRS pathway. The *vc_1637* gene encoding a small hypothetical protein DbfQ is located directly upstream of *dbfR* and *dbfS*. Bottom panel: Domain architecture of DbfQ. (C) Quantification of biofilm biomass over time for WT *V. cholerae,* Δ*dbfQ,* and Δ*dbfS* mutants using time-lapse brightfield microscopy. Points represent averages of *N* = 2 biological replicates and 3 technical replicates, ± standard deviations (SD, shaded regions). (D) As in C for the Δ*dbfS* $dbfR^{D51V}$ and Δ*dbfQ* $dbfR^{D51V}$ strains. (E) Gene neighborhood analysis reveals a module of PepSY domain-containing protein(s) (green), histidine kinase (blue), and response regulator (magenta) genes encoded nearby in the genome. A selected set of species associated with human infections or agriculture is shown. F) Phos-tag analysis of DbfR-SNAP in-gel fluorescence in the presence (+) and absence (Δ) of *dbfS* and *dbfQ*. (G) Quantification of P_{dbfQRS}-*lux* reporter activity for the indicated strains. Data are presented as mean ± SD of peak relative light units (RLU, defined as *lux*/OD_{600}) normalized to the average peak value of WT. Points represent individual replicates of *N* = 2 biological replicates and 3 technical replicates.

DbfQ directly interacts with the sensory domain of DbfS

The genetic results presented above indicate that DbfQ promotes DbfS phosphatase activity. We reasoned that DbfQ could directly interact with the DbfS receptor to modulate its activity. To investigate this possibility, we first examined DbfQ localization. As noted above, DbfQ contains a predicted N-terminal secretion signal and predicted Sec/SPI cleavage site, suggestive of secretion into the periplasm, where it could modulate the periplasmic sensory domain of DbfS. To determine DbfQ localization, we fused DbfQ to mNeonGreen (mNG) and performed confocal microscopy. While endogenously tagged DbfQ was undetectable due to low expression levels, overexpression of DbfQ-mNG revealed localization at the cell periphery, consistent with potential periplasmic localization (Fig. 2A). In contrast, an in-frame deletion of the predicted secretion signal of DbfQ ($dbfQ^{\Delta sec}$-*mNG*) resulted in DbfQ retention in the cytoplasm (Fig. 2A), suggesting that the secretion signal is essential for DbfQ localization. To assess whether DbfQ secretion is required for pathway function, we examined P_{dbfQRS}-*lux* output in the $dbfQ^{\Delta sec}$ background and observed a >15-fold activation of light production (Fig. 2B), indicating that mislocalization of DbfQ results in increased DbfR phosphorylation. We next interrogated the role of DbfQ secretion signal cleavage by introducing bulky aromatic sidechain substitutions at the predicted cleavage residue A31 (A31Y and A31W), a strategy that, for other proteins, has been shown to inhibit processing by Signal Peptidase I (37–39). Western blot of the WT DbfQ-3xFLAG yielded a ~17kDa band corresponding to the expected size of cleaved DbfQ-3xFLAG (Fig. 2C). In contrast, the $DbfQ^{A31W}$-3xFLAG and $DbfQ^{A31Y}$-3xFLAG exhibited higher molecular weight products consistent with the uncleaved, full-length DbfQ (Fig. 2C). The $dbfQ^{A31W}$ and $dbfQ^{A31Y}$

cleavage mutants exhibited 12- and 8-fold increases in P_{dbfQRS}-*lux* reporter activity, respectively, compared to WT (Fig. 2B). Therefore, periplasmic localization and processing of DbfQ is required for its regulatory effect on DbfS activity, and consequently, on DbfR phosphorylation state.

The periplasmic co-localization of DbfQ and the sensory domain of DbfS suggests that DbfQ could directly bind to DbfS to control its output activity. To explore this possibility, we first utilized AlphaFold3, which predicted an interaction between DbfQ and the DbfS sensory domain, with an interface predicted template modeling (ipTM) score of 0.69, a relatively high-confidence value (Fig. 2D). To validate this prediction, we recombinantly expressed and purified DbfQ and the DbfS sensory domain ($DbfS^{SD}$-6xHis) for pull-down assays (Fig. S3A). When supplied alone, DbfQ, which lacked the affinity tag, displayed no binding to Ni-NTA resin, whereas $DbfS^{SD}$-6xHis was bound and subsequently eluted. However, when the two proteins were pre-mixed, DbfQ co-eluted as a complex with $DbfS^{SD}$-6xHis, confirming a direct interaction (Fig. 2E). To measure binding affinity and stoichiometry, we performed microscale thermophoresis (MST). This approach revealed a high-affinity interaction between DbfQ and DbfS, with a dissociation constant (K_d) of 30 nM (Fig. 2F). To determine the stoichiometry of the DbfQ-DbfS interaction, the thermophoretic behavior of labeled DbfQ and unlabeled DbfS was probed using a titration to saturation experiment (40), which indicates a 1:1 stoichiometry between DbfQ and DbfS (Fig. S3B). Collectively, these computational and experimental results establish that DbfQ controls the activity of DbfS via a direct, high-affinity interaction in the periplasm. Combined with our genetic results, we infer that DbfQ binding to DbfS biases the receptor towards phosphatase activity, driving dephosphorylation of DbfR and enabling biofilm dispersal (Fig. 2G).

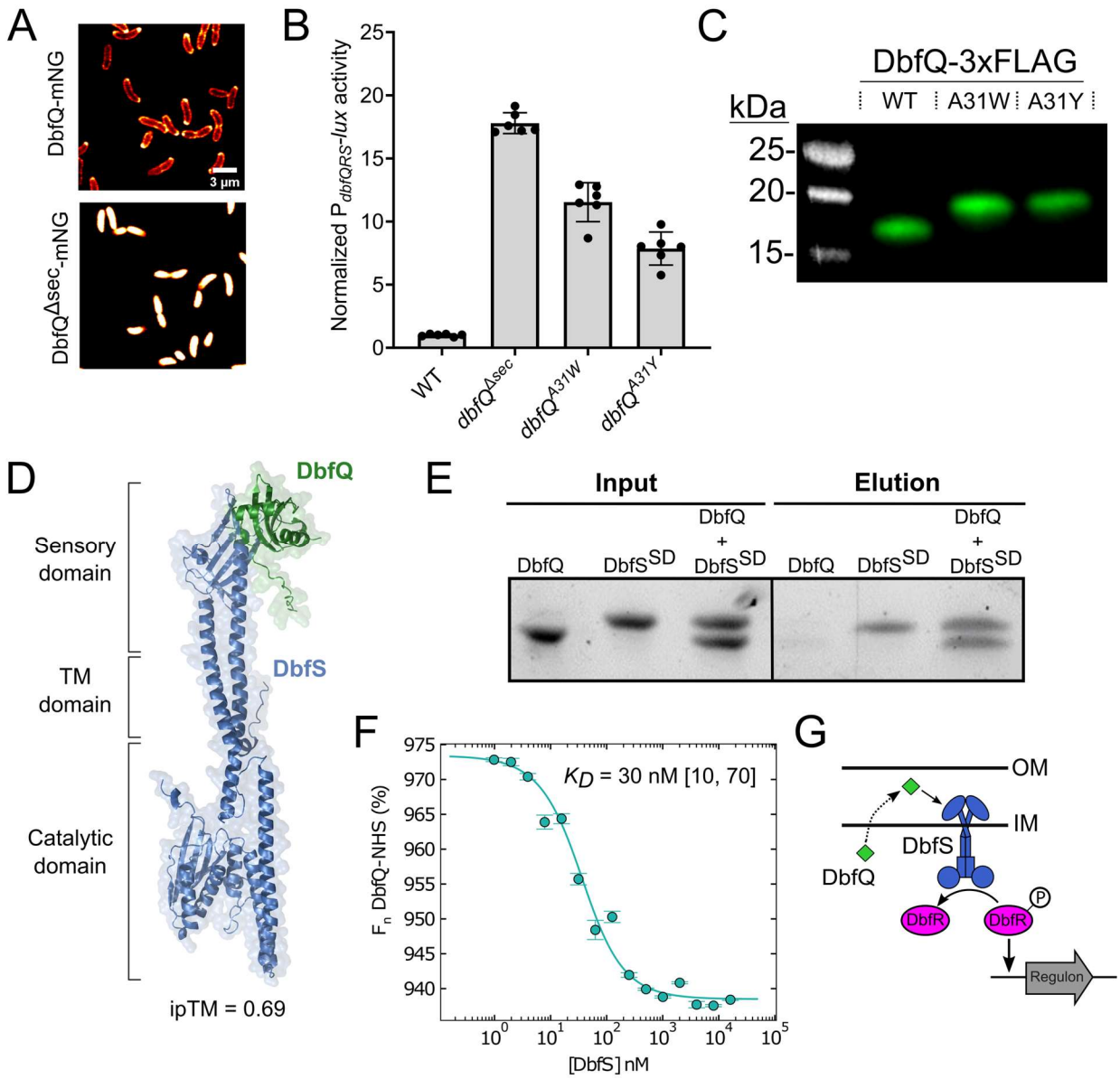

Figure 2. DbfQ directly interacts with the sensory domain of DbfS. (A) Left: Representative confocal microscopy images of DbfQ-mNG in *V. cholerae* expressed from an ectopic locus. Right: As in left panel, except the secretion signal of DbfQ has been removed (*dbfQ*$^{\Delta sec}$-mNG). (B) Quantification of P_{dbfQRS}-*lux* reporter activity for secretion and cleavage mutants. Data are presented as mean ± SD of peak RLU normalized to the average peak value of WT. Points represent individual replicates of N = 2 biological replicates and 3 technical replicates. (C) Western blot analysis of the FLAG-tagged WT DbfQ (cleaved) and the cleavage site mutants DbfQ^{A31W} and DbfQ^{A31Y}. Data are representative of N = 3 biological replicates. (D) Structure of AlphaFold3 predicted interaction between cleaved DbfQ (green) and full-length DbfS (blue), with an ipTM = 0.69. Critical domains of DbfS including sensory, transmembrane (TM), and kinase/phosphatase domains are labeled. (E) SDS-PAGE results of a Ni-NTA pull-down assay between purified DbfQ and the DbfS^{SD}-6xHis. Data are representative of N = 3 independent

experiments. (F) MST dose-response curve used to measure the DbfQ and DbfS^{SD} interaction. DbfQ was covalently labeled with an amine-reactive Red-NHS dye and subsequently titrated against increasing concentrations of unlabeled DbfS while changes in thermophoretic behavior were monitored. Normalized fluorescence (F_n) results were fit with a one-site binding model (95% confidence interval), yielding a dissociation constant of 30 nM [10, 70] [Lower Limit, Upper Limit]. Data are presented as mean ± SD of *N* = 4 independent replicates. (G) Proposed model for the DbfQRS signaling pathway. OM = outer membrane, IM = inner membrane.

DbfQRS activity is sensitive to changes in membrane integrity

A longstanding challenge involving studies of novel bacterial TCSs is identifying the signal(s) that modulate pathway activities. Some TCSs are known to respond to exogenous stimuli, such as nutrients, metals, or host-derived factors (41–43), while others integrate self-produced or intrinsic cues including quorum sensing autoinducers or cell envelope stress (44–47). The *P. aeruginosa* DbfS ortholog, BqsS, was previously shown to be iron-responsive (48), however, we found that supplementation of Fe(II) or Fe(III) did not alter P$_{dbfQRS}$-*lux* reporter output in *V. cholerae* (Fig. S4A). Given the tremendous number of potential exogenous inputs, we decided to focus on identifying any intrinsic factors that modulate DbfQRS activity. We reasoned that such factors could be identified using a transposon mutagenesis approach while monitoring P$_{dbfQRS}$-*lux* reporter activity. Since DbfS exhibits basal phosphatase activity under our laboratory conditions, we sought to identify mutations that increased P$_{dbfQRS}$-*lux* output, reflective of elevated DbfR phosphorylation. Screening of ~20,000 Tn5 mutagenized colonies yielded 54 isolates exhibiting elevated luminescence, which, after sequencing, mapped to 23 loci spanning eight functional categories (Table 1, Table S1, and Fig. S4B). Among the hits, the identification of *dbfQ*::Tn*5* and *dbfS*::Tn*5* validated our screening strategy, as these mutants display increased DbfR phosphorylation (Fig. 1F, G). Strikingly, the largest category of hits (~35%) mapped to genes predicted to be involved in lipopolysaccharide (LPS) biosynthesis. Defects in LPS biosynthesis can profoundly affect the cell envelope by increasing membrane permeability, altering membrane protein expression, and affecting susceptibility to antibiotics (49–51). Consistent with our findings, previous work implicated *vc_1639* (*dbfS*) in resistance to polymyxin B (52), a cationic antimicrobial peptide that disrupts the LPS network and destabilizes the outer membrane. These results suggest a relationship between membrane integrity and DbfQRS pathway activity. To validate this relationship, we first constructed an in-frame deletion of *wavA* (*vc_0223*), the first gene in the LPS core-polysaccharide biosynthesis cluster, which was previously reported to result in truncated LPS lacking O-antigen attachment (53, 54). The Δ*wavA* mutant exhibited a nearly 5-fold increase in luminescence compared to WT strain, consistent with elevated DbfR phosphorylation (Fig. 3A). Introducing the phospho-dead *dbfR*^{D51V} allele into Δ*wavA* background suppressed light production to below that of WT, confirming that modifications in LPS enhance pathway activation specifically via DbfR phosphorylation, and not via parallel transcriptional control of the *dbfQRS* promoter. To further substantiate the link between membrane stress and DbfQRS activation, we treated

WT cells with sub-lethal concentrations of the membrane-targeting antibiotic polymyxin B and measured P_{dbfQRS}-*lux* reporter output. This treatment led to a dose-dependent increase in luminescence, reaching a maximum of 6-fold induction at the highest concentration tested (Fig. 3B). Similarly, exposure to thymol, an antimicrobial compound known to disrupt membrane integrity (55), produced up to an 8-fold increase in luminescence (Fig. 3C). In contrast, the *dbfR*^{D51V} strain failed to induce light production under either treatment, demonstrating that DbfR phosphorylation is a direct readout of outer membrane stress. Possible mechanisms through which the DbfQRS pathway senses outer membrane damage are numerous, including that DbfQ or DbfS senses some characteristic of envelope stress that modulates their interaction. Defining the precise mechanism underlying this response will be the topic of future work.

Table 1: Functional distribution of transposon mutagenized genes with increased DbfQRS activity

Primary function*	No. of genes	% of genes
LPS biosynthesis	8	35
Transcription, Translation, and DNA repair	6	26
Transport	2	9
Signal transduction (*dbfQ* and *dbfS*)	2	9
Metabolism	1	4
Hypothetical proteins	2	9
Phage shock protein	1	4
Virulence	1	4
Total	23	100

*Assigned by KEGG Orthology Database

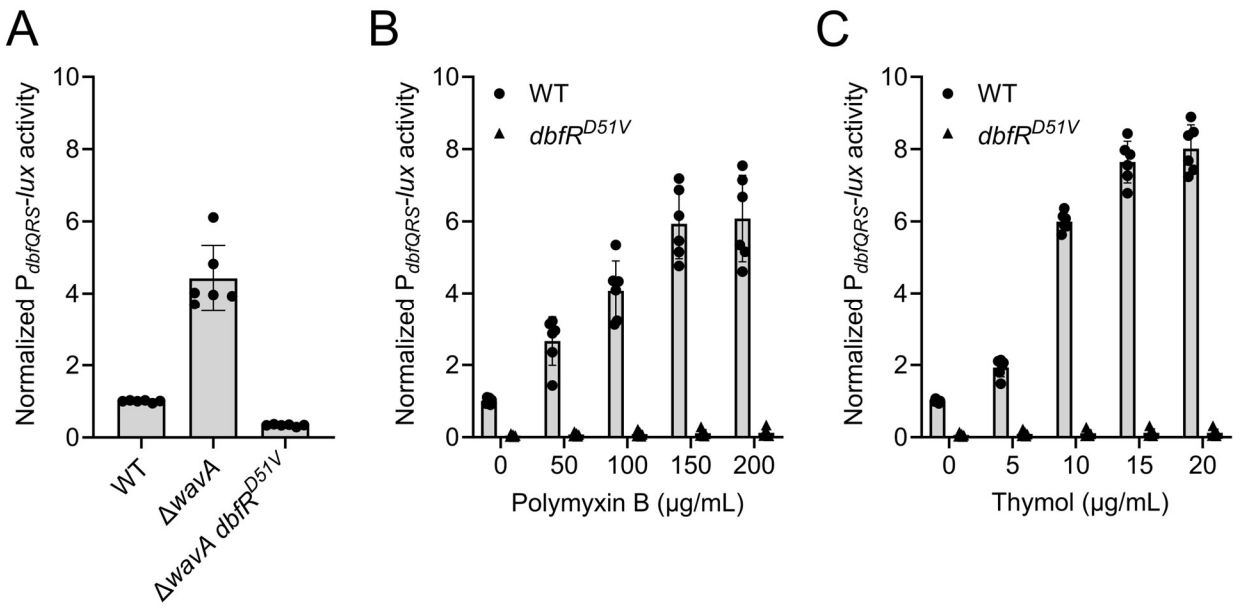

Figure 3. DbfQRS activity is sensitive to membrane disruption. (A) Quantification of P_{dbfQRS}-*lux* reporter activity for the indicated strains. Data are presented as mean ± SD of peak RLU normalized to the average peak value of WT. Points represent individual replicates of *N* = 2 biological replicates and 3 technical replicates. (B) As in A for the indicated strains under polymyxin B treatment. (C) As in A for the indicated strains under thymol treatment.

The DbfQRS pathway activates biofilm formation while downregulating metabolic processes

Our next goal was to characterize the effects of DbfQRS signaling on downstream gene expression. To define the DbfR regulon, we performed RNA sequencing under conditions where DbfR was either constitutively dephosphorylated or phosphorylated. We began by comparing the transcriptome of WT *V. cholerae* to the phospho-dead *dbfR*^{D51V} strain. This strain displayed modest transcriptional changes, with 54 genes exhibiting differential expression ($Log_2FC > \pm 1.0$ and *P*-value < 0.05) (Fig. S5A, Dataset S1). In contrast, when DbfR was phosphorylated (using the Δ*dbfS* mutant strain), we observed a dramatic shift in gene expression, with 12% of genomic loci (*N* = 540 genes) exhibiting differential expression (Fig. 4A, Dataset S2). These results confirm that DbfR phosphorylation drives large-scale transcriptional reprogramming. As expected, the Δ*dbfQ* mutant, which also exhibits elevated DbfR phosphorylation (Fig. 1F, G), displayed a similar transcriptional profile to the Δ*dbfS* strain (R = 0.93) (Fig. 4B, Fig. S5B and Dataset S3).

To gain functional insights into the genes regulated by phospho-DbfR, we performed a KEGG pathway enrichment analysis. This analysis revealed significant

downregulation of genes involved in central metabolic pathways, including the tricarboxylic acid (TCA) cycle and oxidative phosphorylation, as well as genes implicated in purine/pyrimidine metabolism, amino acid metabolism, and the biosynthesis of secondary metabolites (Fig. 4C, Dataset S4). These results are consistent with our finding that the Δ*dbfS* and Δ*dbfQ* mutants exhibited a reduced growth rate compared to WT (Fig. S1A). Beyond metabolic changes, genes involved in flagellar assembly were also downregulated under phospho-DbfR conditions, suggesting that the pathway controls motility in addition to biofilm formation (Fig. 4A, D). Soft-agar motility assays confirmed that both Δ*dbfS* and Δ*dbfQ* strains exhibited significantly decreased motility compared to WT, though not to the extent of the Δ*flaA* mutant lacking the major flagellin subunit (Fig. 4D and Fig. S6). On the other hand, significantly upregulated pathways in the Δ*dbfS* and Δ*dbfQ* transcriptomes included genes encoding vibrio exopolysaccharide (*vps*) biofilm matrix components, peptidoglycan biosynthesis, and mismatch repair proteins (Fig. 4A, C). Collectively, these results suggest that DbfR activation biases *V. cholerae* towards a sessile biofilm state, while simultaneously slowing growth by reducing metabolic processes. We propose that entering this state could prepare cells for environmental challenges.

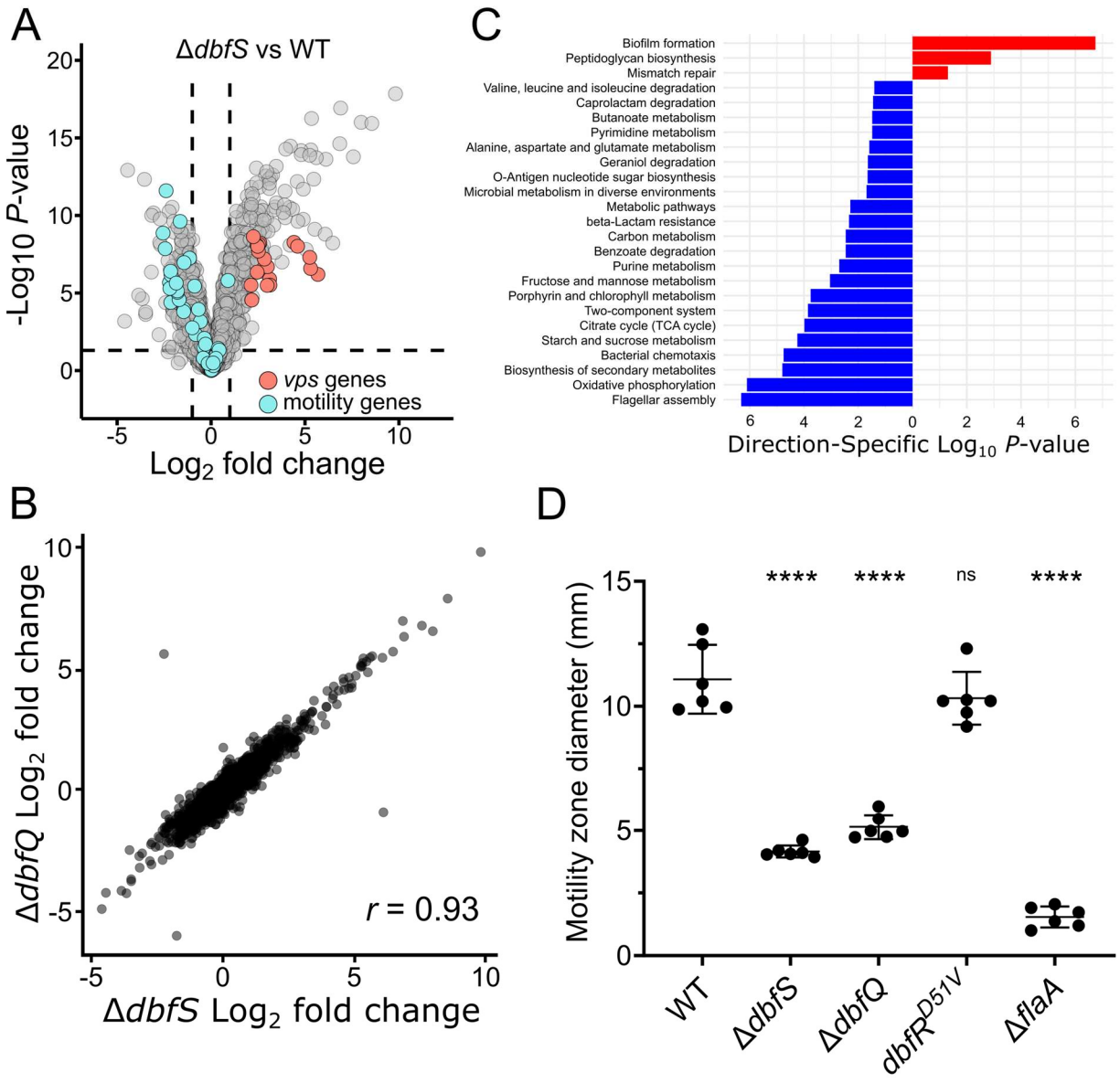

Figure 4. The DbfQRS pathway regulates the expression of metabolic and lifestyle genes. (A) Volcano plot comparing fold changes and *P*-values for gene expression in the Δ*dbfS V. cholerae* strain compared to WT. *vps* and motility genes are highlighted in orange and cyan, respectively. The horizontal dotted line represents a -Log_{10} *P*-value of 0.05, and left and right vertical dashed lines represent Log_2 fold changes of −1 and 1, respectively. Samples were collected at OD_{600} = 0.1 and *N* = 3 biological replicates for each strain. Complete datasets are available in Dataset S2. (B) Comparison of Log_2 fold changes in gene expression for the Δ*dbfS* and Δ*dbfQ* mutants. *r* = Pearson's correlation coefficient. Complete datasets are available in Dataset S2 and S3. (C) Significantly enriched KEGG pathways (*P* < 0.05) in the Δ*dbfS* mutant strain. Differentially regulated genes (false discovery rate < 0.05) were assigned to pathways using the "kegga" functionality in *limma* R package (56). Red bars represent upregulated pathways, and blue bars represent downregulated pathways. (D) Motility zone measurement for

the indicated strains after 10 hours of incubation. Points represent individual replicates of $N = 6$ biological replicates. Statistical analyses were performed using unpaired, two-sample t-tests with a 95% confidence interval (****, $P < 0.0001$; ns, not significant).

DbfR phosphorylation drives biofilm formation by increasing c-di-GMP levels

The simultaneous upregulation of *vps* gene expression and downregulation of motility factors observed in our transcriptomic analysis could be manifested by changes in cyclic dimeric GMP (c-di-GMP) levels. C-di-GMP is a widespread bacterial second messenger molecule which controls motile-to-sessile transitions by repressing motility and promoting biofilm matrix production in *V. cholerae* and other organisms (57). To assess intracellular c-di-GMP levels under phospho-DbfR conditions, we introduced an established riboswitch-based c-di-GMP fluorescence reporter into the Δ*dbfS* mutant (58, 59). Reporter output in this strain was ~40% higher than in WT, confirming that DbfR phosphorylation is associated with elevated intracellular c-di-GMP levels (Fig. 5A). Intracellular c-di-GMP levels are regulated by opposing enzymatic activities: diguanylate cyclases synthesize c-di-GMP via GGDEF domains, while phosphodiesterases degrade c-di-GMP through EAL or HD-GYP domains (60, 61). Of note, *V. cholerae* encodes 62 such c-di-GMP metabolic enzymes (62), raising the question of which specific enzyme(s) drive the observed c-di-GMP increase upon DbfR phosphorylation. Examination of RNA-sequencing results was not particularly revealing, as widespread changes in the expression of c-di-GMP-metabolizing enzymes were observed in the Δ*dbfS* mutant (Fig. 5B, Dataset S2).

To pinpoint the critical enzyme(s) responsible for elevated c-di-GMP in the Δ*dbfS* background, we pursued an unbiased mutagenesis screen that exploits the distinctive colony morphology of the Δ*dbfS* mutant. This strain exhibits a wrinkled, “rugose” phenotype consistent with elevated biofilm matrix production, thereby providing a clear phenotypic readout for its hyper-biofilm formation (Fig. 5C). We mutagenized the Δ*dbfS* strain with the Tn*5* transposase, screened ~20,000 colonies and identified 183 suppressor mutants exhibiting a smooth colony morphology. Sequencing these mutants revealed that 81% harbored disruptions in *vps* genes (Table S2) within the biofilm matrix operons, confirming that the rugose to smooth phenotypic transition reflects loss of biofilm matrix production (Fig. 5D, Left). Each *vps* gene was disrupted ~8 times on average, validating the comprehensiveness of our screen (Fig. 5D, Middle). We also identified other established biofilm regulators, including the master biofilm transcription factors *vpsR* and *vpsT*, the quorum-sensing regulator *luxO*, and the alternative sigma factor *rpoN* (Fig. 5D, Right). Most notably, a single c-di-GMP metabolizing enzyme, *cdgL* (*vc_2285*), emerged from the screen. This diguanylate cyclase also appeared as the most highly upregulated c-di-GMP metabolizing enzyme in our Δ*dbfS* transcriptomic dataset (Fig. 5B), suggesting it could mediate elevated c-di-GMP upon DbfR phosphorylation. To test this possibility, we deleted *cdgL* in the Δ*dbfS* background, which reduced peak biofilm

formation to below that of WT, and restored biofilm dispersal, demonstrating that CdgL is essential for the hyper-biofilm phenotype of the Δ*dbfS* strain (Fig. 5E). To determine if CdgL links DbfR phosphorylation to elevated c-di-GMP levels, we introduced the c-di-GMP reporter into the Δ*dbfS* Δ*cdgL* double mutant. As expected, the ~40% increase in c-di-GMP levels observed in the Δ*dbfS* strain (Fig. 5A) was nearly abolished in the Δ*dbfS* Δ*cdgL* double mutant, which exhibited only a modest (~12%) increase relative to the Δ*cdgL* single mutant (Fig. 5F). Of note, we found that the Δ*cdgL* single mutant exhibited a >20% reduction in basal c-di-GMP reporter output and reduced peak biofilm biomass relative to the WT (Fig. S7A, B), demonstrating that CdgL also contributes to baseline c-di-GMP synthesis even when DbfR is dephosphorylated. Taken together, our results suggest that phosphorylated DbfR activates c-di-GMP synthesis in large part through *cdgL* upregulation, driving a transcriptional program favoring a sessile biofilm state.

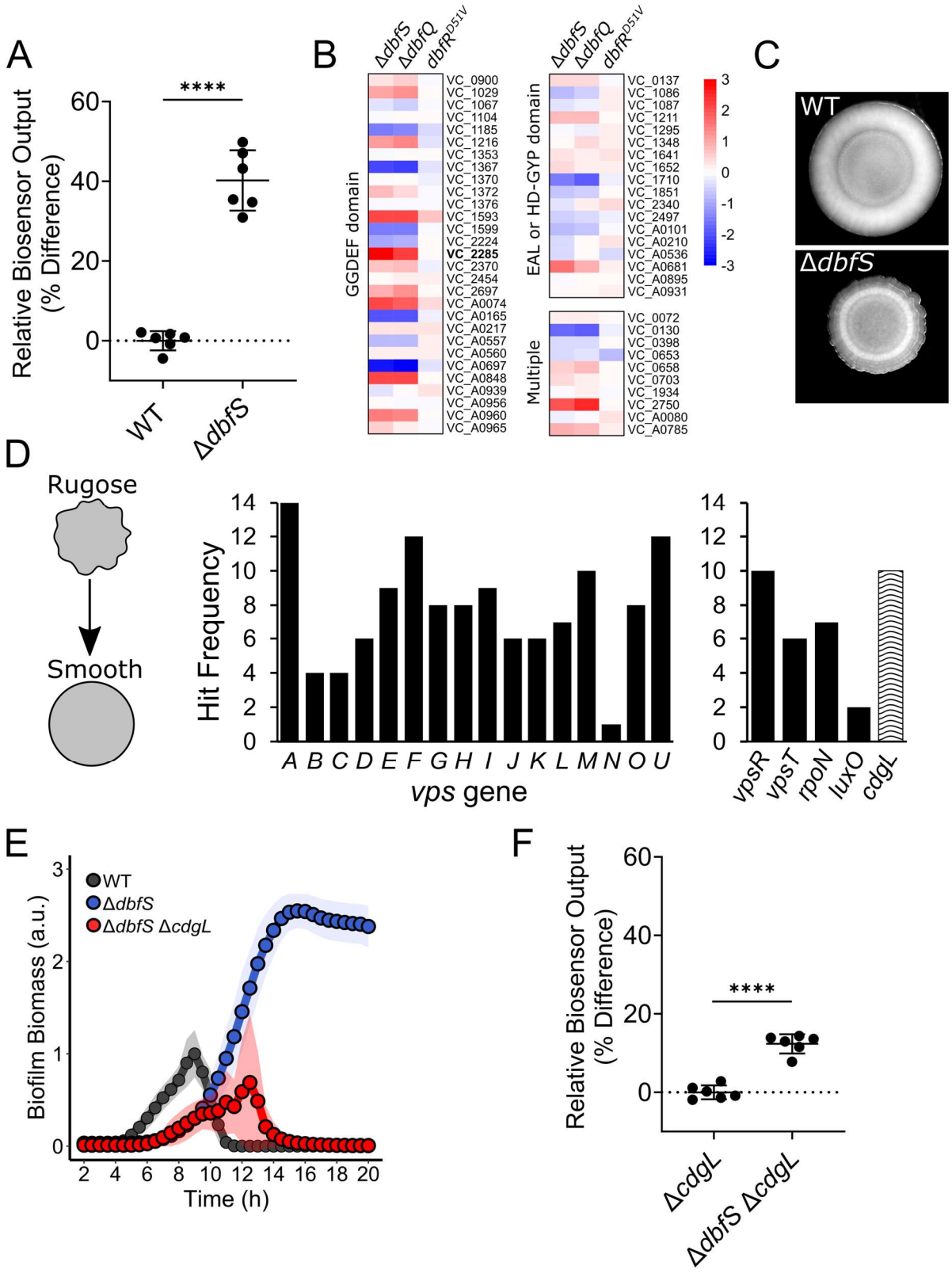

Figure 5. DbfR phosphorylation drives increased c-di-GMP levels via upregulation of *cdgL*. (A) Relative c-di-GMP reporter output for the WT and Δ*dbfS* strains, expressed as the mean ± SD of percentage difference relative to the WT control. Points represent individual replicates of *N* = 2 biological replicates and 3 technical replicates. Statistical analyses were performed using unpaired, two-sample t-tests with a 95% confidence interval (****, *P* < 0.0001). (B) Heatmap of RNAseq results for c-di-GMP metabolizing enzymes in the indicated strains. Genes are grouped by the presence of GGDEF domain (diguanylate cyclase), EAL or HD-GYP domains (phosphodiesterase), or multiple catalytic domains, potentially representing bifunctionality. Color bar represents Log_2 fold changes. *VC_2285* (*cdgL*) is bolded for ease of identification. (C) Stereomicroscope images of WT and Δ*dbfS* colony morphologies. (D) Left: Schematic of mutagenesis screen. Middle: Hit frequency for genes in the *vps-I* and *vps-II* operons. Right panel: Hit frequency for selected regulators of biofilm formation. All screen hits are reported in Table S2. (E) Quantification of biofilm biomass for WT, Δ*dbfS*, and Δ*dbfS* Δ*cdgL* strains using time-lapse brightfield microscopy. Points represent averages of *N* = 2 biological replicates and 3 technical replicates, ± SD (shaded regions). (F) As in A for the Δ*cdgL* and Δ*dbfS* Δ*cdgL* double mutant. Reporter output is normalized to the Δ*cdgL* strain.

Constitutive DbfR phosphorylation compromises *V. cholerae* fitness in an animal model of infection

Given the dramatic transcriptomic changes, reduced growth rate, and commitment to the biofilm state observed upon DbfR phosphorylation, we wondered how activation of this pathway relates to *V. cholerae* fitness, particularly during infection. To assess fitness, we conducted competition assays in LB media and in the infant mouse model of *V. cholerae* infection. We competed WT *V. cholerae* against the dephosphorylated *dbfR*^{D51V} strain, as well as the Δ*dbfS* and Δ*dbfQ* strains that exhibit elevated DbfR phosphorylation. For both *in vitro* and *in vivo* assays, the competitive index (CI) for *dbfR*^{D51V} was around 1, indicating that inactivation of DbfR phosphorylation does not impair *V. cholerae* fitness in media or in the animal (Fig. 6A, B). In contrast, the Δ*dbfS* and Δ*dbfQ* mutants were significantly outcompeted by the WT strain under both conditions, with CI values at least 10-fold lower than the *dbfR*^{D51V} strain (Fig. 6A, B). Complementation of the Δ*dbfS* and Δ*dbfQ* mutants restored fitness in both conditions. We wondered whether the disadvantage of the phospho-DbfR strains was due to their commitment to the biofilm state. To test this possibility, we performed competition experiments with the Δ*dbfS* Δ*cdgL* mutant, which, as shown above, disconnects biofilm regulation from DbfR-phosphorylation. We note that the Δ*dbfS* Δ*cdgL* strain exhibits slower growth than the WT, though its growth defect is less severe than the Δ*dbfS* single mutant (Fig. S7C). Consistent with this observation, we found that the Δ*dbfS* Δ*cdgL* strain was also significantly outcompeted in culture and in mice (Fig. 6A, B). Given that 540 genes are differentially expressed in the Δ*dbfS* mutant (Fig. 4A), our results suggest that other components of the regulon, unrelated to the biofilm lifecycle, are responsible for the

competitive disadvantage *in vitro* and *in vivo*. Overall, our results demonstrate that activation of the DbfQRS pathway negatively impacts the fitness of *V. cholerae* both in culture and in mice. Importantly, our findings highlight that the DbfQRS pathway could serve as a suitable target for the development of novel anti-infectives that function by reducing *V. cholerae* fitness.

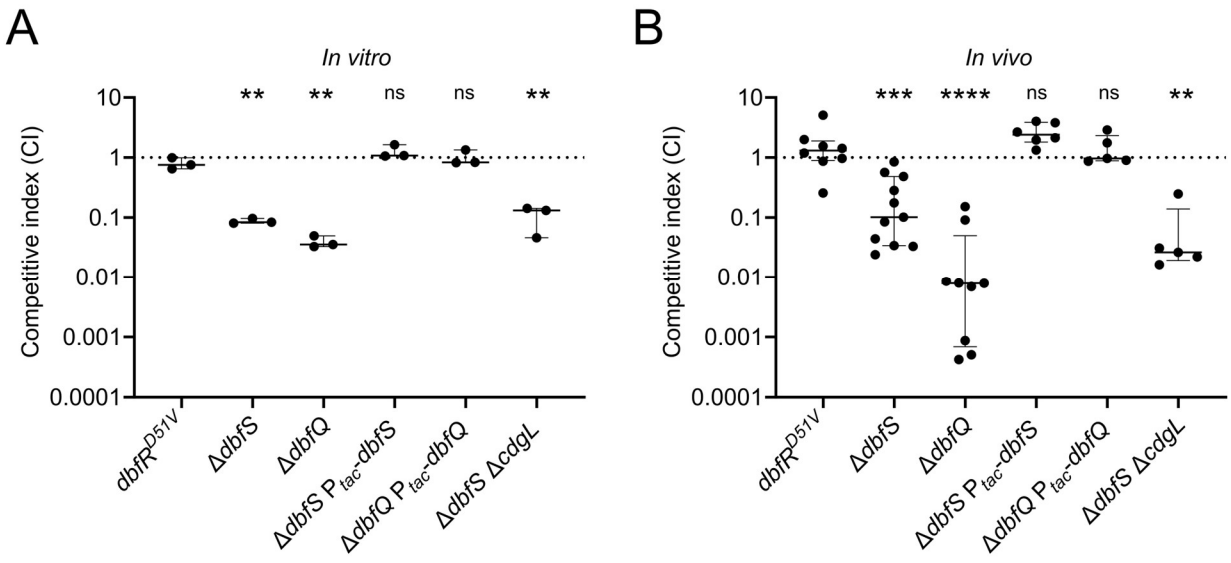

Figure 6. Activation of the DbfQRS pathway results in a competitive disadvantage *in vitro* and *in vivo*. (A) *In vitro* competition assay. WT (*lacZ*⁻) *V. cholerae* were competed against the indicated strains at a 1:1 ratio in LB medium for 24 hours. Data are displayed as the median with interquartile ranges. Points represent individual replicates of $N = 3$ biological replicates. Statistical analyses were performed using unpaired, two-sample t-tests with a 95% confidence interval. (B) *In vivo* competitive colonization assay. WT (*lacZ*⁻) was competed against the indicated strains at a 1:1 ratio in the infant mouse small intestine for 24 hours. Data are presented as a single data point per mouse, along with median and interquartile range for each condition. Statistical analyses were performed using the Mann-Whitney U test. In both assays, competitive indices (CI) were calculated as the ratio of output to input of the mutant strain relative to the WT. (*, $P < 0.05$; **, $P < 0.01$; ***, $P < 0.001$, ****, $P < 0.0001$; ns, not significant).

Discussion

The current work represents an initial characterization of a novel class of bacterial TCSs involving a small, secreted protein which directly modulates receptor activity. We provide a comprehensive investigation of the DbfRS TCS in *V. cholerae* – encompassing its input signals, the role of DbfQ as pathway regulator, and downstream effects of DbfR phosphorylation. Using multidisciplinary approaches, we demonstrate that DbfQ controls the activity of DbfS via a direct, high-affinity interaction that is central to pathway regulation. Indeed, the dynamic balance in the opposing kinase and phosphatase

activities of DbfS calibrates the phosphorylation state of DbfR, which in turn determines *V. cholerae*'s decision to disperse or commit to a biofilm state. We reveal that defects in LPS biosynthesis or the presence of membrane-targeting agents elevate DbfR phosphorylation, implicating the pathway in responding to outer membrane perturbations. We propose that membrane damage could lead to the loss of periplasmic components (e.g. leakage of DbfQ), or the release of other mechanical and biochemical cues that might be directly detected by DbfQ or DbfS. These signals could function to disrupt the DbfQ-DbfS interaction, biasing the system towards DbfR phosphorylation. Cells could then commit to the biofilm-associated state, potentially as a stress-driven protective response. Future investigations will be required to resolve whether DbfQRS directly senses perturbations in membrane integrity or responds to secondary stress signals.

The DbfQRS pathway exerts pleiotropic control over the biofilm lifecycle, metabolic activities, motility, and peptidoglycan biosynthesis, underscoring its wide-ranging influences on *V. cholerae* physiology. Strikingly, constitutive activation of the pathway imposes a fitness cost, compromising *V. cholerae* growth and colonization. Consistent with this finding, we note that a previous attempt to generate an in-frame deletion of *dbfS* in a different *V. cholerae* isolate was unsuccessful, suggesting that constitutive DbfR activation may even be lethal in some strain backgrounds (63). In the current study, we find that the growth defect observed upon pathway activation is not due to the costs associated with elevated biofilm production. Thus, we propose that the fitness cost of DbfQRS hyperactivity is likely to arise from transcriptional downregulation of metabolic processes. Pinpointing the pathways controlled by DbfR that impact growth will be the subject of future studies.

Despite the costs of DbfQRS hyperactivation, the widespread conservation of this pathway suggests it confers a selective advantage under specific conditions. Given that DbfQRS responds to outer membrane stresses, its activation may serve as a regulatory mechanism that prioritizes stress adaptation over cellular activity. By reprogramming cellular processes (i.e. enhancing biofilm formation while downregulating metabolism, motility, and growth), DbfQRS activation likely benefits *V. cholerae* in hostile environments where survival takes precedence over rapid proliferation. For example, downregulation of metabolic processes may conserve energy during nutrient deprivation while biofilm formation could provide protection against environmental stressors such as predation or antimicrobials. The DbfQRS pathway is distinct in that, unlike many TCSs that regulate specific aspects of bacterial adaptation, it orchestrates a broad, pleiotropic shift in cellular physiology — encompassing biofilm regulation, metabolism, motility, and cell envelope integrity. Such expansive regulatory control underscores its unique role as a master switch for multiple adaptation strategies in adverse environments.

In summary, our work reveals that the DbfQRS pathway integrates membrane stress signals with global regulatory responses, thereby linking environmental challenges

to adaptive lifestyle transitions in *V. cholerae*. More broadly, understanding how stress-responsive TCSs like DbfQRS orchestrate bacterial adaptation may reveal novel antimicrobial strategies that exploit the inherent trade-offs in bacterial stress adaptation. Because DbfQRS influences a global profile of gene expression, interventions targeting this pathway might be effective against multiple facets of bacterial physiology. By hyperactivating the pathway to force *V. cholerae* into a low-fitness state, we could exploit its pleiotropic trade-offs to curb bacterial resilience. Given the widespread conservation of *dbfQRS*-like modules across bacterial phyla, it is likely that similar regulatory principles extend beyond *V. cholerae*. Future studies should explore whether this pathway plays a comparable role in other clinically and environmentally relevant bacteria. Examining the function of DbfQRS homologs in diverse species could reveal conserved and species-specific regulatory strategies, offering insight into how different bacteria fine-tune stress responses. Additionally, structural and biochemical characterization of DbfQ orthologs could determine whether their mode of receptor modulation is universally conserved or has evolved to accommodate distinct signaling contexts. A deeper understanding of the DbfQRS family may not only refine our current models of bacterial signaling networks but also uncover new targets for antimicrobial interventions by disrupting stress adaptation mechanisms in pathogenic bacteria.

Materials and Methods

Bacterial strains, reagents, and cloning

The *V. cholerae* parent strain used in this study was O1 El Tor biotype C6706str2. *E. coli* S17 and Top10 were used to transfer plasmids into *V. cholerae* by conjugation. A complete list of strains used in this study is provided in Table S3. For passaging and cloning, *V. cholerae* and *E. coli* strains were cultivated in lysogeny broth (LB) supplemented with 1.5% agar or in liquid LB with shaking at 30°C and 37°C, respectively. Unless otherwise specified, antibiotics were used at the following concentrations: polymyxin B, 50 µg/mL; kanamycin, 50 µg/mL; spectinomycin, 200 µg/mL; streptomycin, 400 µg/mL, chloramphenicol, 2 µg/mL; and gentamicin, 15 µg/mL; ampicillin, 100 µg/mL. For microscopy, luminescence quantifications, and c-di-GMP reporter measurements, *V. cholerae* strains were grown in M9 minimal medium supplemented with dextrose and casamino acids (1x M9 salts, 100 µM $CaCl_2$, 2 mM $MgSO_4$, 0.5% dextrose, 0.5% casamino acids). When required, *L*-arabinose (Thermo Fisher Scientific) was added at a concentration of 0.2% from the start of assays.

All genetic modifications were generated by replacing genomic DNA with linear DNA introduced via natural transformation, as described previously (64–66). PCR amplification was performed with iProof (Bio-rad) or Q5 DNA polymerase (New England Biolabs). Sanger sequencing (Azenta) was used to verify genetic alterations. Genomic DNA from recombinant strains was used as templates for generating DNA fragments as needed. Gene deletions were generated in-frame to remove the entire coding sequences, except for *dbfS* and *dbfR*, which overlap in their operon. For these genes, an internal

portion of each gene was deleted to avoid perturbing the adjacent gene. To construct *dbfQ-3xFLAG* at its native locus, a C-terminal 3xFLAG epitope tag was inserted immediately upstream of the *dbfQ* stop codon. Oligonucleotides and synthetic linear DNA g-blocks were ordered from IDT and are reported in Table S4.

Microscopy and image analysis

The *V. cholerae* biofilm lifecycle was monitored by time-lapse brightfield microscopy as described previously (67). Briefly, single colonies of *V. cholerae* were inoculated into 200 µl of LB medium in 96-well plates covered with a breathe-easier membrane (USA Scientific Inc) and grown overnight at 30°C with constant shaking. The following morning, overnight cultures were diluted ~1:200,000 in M9 minimal medium to achieve a final OD_{600} of ~1 x 10^{-5}. Diluted cultures were statically grown at 30°C in 96-well polystyrene microtiter plates (Corning) in an Agilent Biospa robotic incubator which transferred microtiter plates for brightfield imaging at 30-min intervals over a 24-h period. Image acquisition was performed using the Agilent Biotek Cytation 1 imaging plate reader equipped with a 10x air objective (Olympus Plan Fluorite, NA 0.3) or a 4x air objective (Olympus Plan Fluorite, NA 0.13), controlled by the Biotek Gen5 (Version 3.12) software. Quantifications of biofilm biomass were performed based on the principle that biofilms scatter light to a greater degree than planktonic cells in low-magnification brightfield images. To segment biofilms within brightfield images, first pixel intensities were inverted, local contrast was normalized, images were blurred with a Gaussian filter, and a fixed threshold was applied allowing for the differentiation of biofilms from background. The resulting binarized image masks were then applied to the raw images to determine the total light attenuated by biofilms with the field of view, yielding our biofilm biomass metric. Peak biofilm biomass corresponding to the maximum value recorded in each time-lapse replicate. In all cases, biomass values were normalized to the peak biomass of the control strain to account for day-to-day variability and for ease of comparison between strains/conditions. Image analyses were performed using the Julia programming language (version 1.11.1). Plotting was performed in RStudio (version 4.4.1) (68) using the ggplot2 package (69).

Fluorescence microscopy used to investigate DbfQ localization was performed on a DMI8 Leica SP-8 point scanning confocal microscope driven by LasX software. For imaging, strains harboring DbfQ fusions to mNG were first grown in M9 medium to OD_{600} = 0.6, at which point cultures were diluted 1000x and inoculated into glass-bottomed 96-well plates (Mattek). Cells were then allowed to attach for 1 h before imaging. Microscopy was performed with a 63x objective (Leica, NA = 1.20), along with a digital zoom of 5x. A tunable white-light laser (Leica; model #WLL2; excitation window = 470–670 nm) set to 503 nm was used to excite mNG fluorescence. Light was detected using GaAsP spectral detectors (Leica, HyD SP), and timed gate detection and frame averaging were employed to minimize background signal.

Gene neighborhood analysis

To assess if PepSY domain-containing proteins (PDPs) are frequently found in the genomic proximity of histidine kinases (HKs) and/or response regulators (RRs) in bacterial genomes, we performed a non-comprehensive screen using a large database of proteins from InterPro (70). First, we downloaded gene IDs and organism IDs for three

sets of proteins: (1) ~1.2M proteins containing the HK domain (IPR005467), (2) ~1.6M proteins containing the RR domain (IPR001789), and (3) ~17K proteins containing only the PepSY domain (IPR025711). Gene IDs for each protein were of the form "<genome-ID>_<gene-number>". Second, using a custom Python script, we parsed the above gene IDs and identified all pairs of PDP and HK/RR genes that lie within 4-gene numbers in the same genome. This stringent cutoff was not selected to be comprehensive, but instead to reveal genomes where three gene classes are closely positioned on the genome. Third, to allow an assessment of our result, we estimated the null probability of a PDP lying near an HK/RR by assuming an average circular bacterial genome of 4000 genes, and one copy each of a PDP and an HK/RR distributed randomly in this genome. The observed frequency of a PDP and an HK/RR in proximity was found to be >60-fold higher than null.

To identify which taxa had a PDP and an HK/RR within a 4-gene vicinity, we used organism IDs from the shortlisted set above and determined their taxonomic order, class and phylum using the tree of life found in the STRING database (string-db.org/cgi/download) (71). The order Vibrionales (containing genus *Vibrio*) made up 0.8% of the dataset. Therefore, all taxa with a representation of ≥ 0.8% were shown in the table (Fig. S2). Finally, for a handpicked set of species relevant to human health and agriculture, gene neighborhood data was displayed (Fig. 1E) using the FlaGs pipeline (72) with the following RefSeq IDs of PDPs as input and default parameters: WP_001165432.1, WP_011080671.1, WP_003090497.1, WP_000780501.1, WP_004201003.1, and WP_003592804.1.

Phos-tag gel analysis.

To monitor DbfR and phospho-DbfR via SDS-PAGE, phos-tag gel experiment was carried out as described previously (30), with some minor adjustments. Briefly, the endogenous *dbfR* gene was replaced with *dbfR-SNAP* in Δ*dbfS* and Δ*dbfQ* Δ*dbfS* strains, and an arabinose-inducible P_{BAD}-*dbfS* was introduced at an ectopic locus (*vc_1807*). Overnight cultures of each strain were diluted 1:1,000 in 3 mL of LB and grown at 30°C with shaking to an OD_{600} of ~0.6, after which 1 µM SNAP-Cell TMR Star (New England Biolabs) was added to label the SNAP tag. Cultures were subsequently divided into two tubes: 0.2% *L*-arabinose was added to one tube to induce DbfS production, while the other tube was left uninduced. The cultures were returned to 30°C with shaking and after 1-h incubation, 1 mL of the cultures were harvested by centrifugation (13,000 rpm, 1min). Pelleted cells were subsequently lysed in 40 µL of Bug Buster (EMD Millipore, #70584–4) for 5 min at 25°C with intermittent vortexing. Lysates were solubilized in 1.5x SDS/PAGE buffer for 5 min and samples were immediately loaded onto a cold 7.5% SuperSep Phos-tag gel (50 µM) (FUJIFILM Wako Pure Chemical; 198-17981). Electrophoresis was carried out at 80V at 4°C for ~1 h. Gel images were captured on the FluorChem E Imaging System (ProteinSimple)

Quantification of P_{dbfQRS}-*lux*

To quantify the transcriptional activity of the *dbfQRS* promoter as a proxy for DbfR phosphorylation, we constructed a P_{dbfQRS}-*lux* reporter by fusing the *dbfQRS* promoter to the *luxCDABE* luciferase operon from *Photorhabdus* (73). All strains used in this assay harbored a *vpsL* deletion to eliminate biofilm-related interference with luminescence and optical density measurements. Unless indicated otherwise, overnight cultures of strains

harboring the P_{dbfQRS}-*lux* reporter were diluted to OD_{600} of ~1 x 10^{-5} in fresh M9 medium in 96-well plates. Optical density at 600 nm (OD_{600}) and luminescence intensity (*lux*) from P_{dbfQRS}-*lux* were measured simultaneously at 30-min or 1-h time intervals over a 24-h period using the Agilent Biotek Cytation 1 Plate Reader, driven by the Biotek Gen5 software. For quantification of P_{dbfQRS}-*lux* reporter output in the presence of antimicrobials or iron, cultures were adjusted to a starting OD_{600} ~ 0.1 at the onset of assay. For antimicrobials assay, overnight cultures were diluted in M9 medium supplemented with increasing concentrations of polymyxin B or thymol. For iron supplementation assay, overnight cultures were diluted in M9 medium supplemented with 100 µM $FeCl_2$ or $FeCl_3$, followed by a shortened 2-h assay to minimize Fe(II) oxidation.

Transposon mutagenesis screens

Two independent Tn5 transposon mutagenesis screens were performed: (1) to identify mutations activating P_{dbfQRS}-*lux*, and (2) to identify suppressors of colony rugosity in the Δ*dbfS* background. In both cases, transposon mutagenesis was carried out identically: *E coli* strain S17 harboring the Tn5::*kan* transposase plasmid was conjugated with the specified parent *V. cholerae* strains. Conjugation was allowed to proceed for two hours at 37° C on LB agar plates without selection. The short incubation ensured limited appearance of "sister" mutants derived from cell divisions following transposon insertion. Conjugations were collected with a sterile loop, resuspended in liquid LB media, and plated on selective media. Transposon insertion mutants were selected on LB agar plates supplemented with streptomycin (to kill *E. coli*) and kanamycin (to select for transposon integration). For the P_{dbfQRS}-*lux* screen, mutant colonies with visibly increased luminescence, as observed on a FluorChem E imager, were isolated, grown overnight, and arrayed into 96-well plates for quantification of P_{dbfQRS}-*lux* reporter activity as described above. Mutants exhibiting significantly elevated luminescence compared to WT control were selected for further analysis. In the Δ*dbfS* colony rugosity suppressor screen, mutants displaying a smooth colony morphology (rugose-to-smooth transition) were identified by visual inspection and selected for sequencing. The locations of transposon insertions in both screens were determined using arbitrary PCR (Table S4) followed by Sanger sequencing (Azenta) (74).

Western blotting of DbfQ-3xFLAG

For western blotting to assess DbfQ cleavage, cultures of strains expressing DbfQ-3xFLAG and its cleavage variants were grown to OD_{600} = 1.0, then harvested by centrifugation for 1 min at 13,000 rpm. The resulting pellets were flash frozen, thawed, and lysed for 10 min at 25°C by resuspension to OD_{600} = 1.0 in Bug Buster (EMD Millipore) supplemented with 0.5% Triton-X, 50 µg/mL lysozyme, 25 U/mL benzonase nuclease, and 1 mM phenylmethylsulfonyl fluoride (PMSF). 1x SDS-PAGE buffer (final) was then added and allowed to incubate for 1 h at 37°C before loading into 4–20% Mini-Protein TGX gels (Bio-Rad). Electrophoresis was performed at 200 V for 30 min. Protein transfer onto PVDF membranes (Bio-Rad) was then performed for 1 h at 4°C at 100 V in transfer buffer (25 mM Tris, 190 mM glycine, 20% methanol). Membranes were blocked for 1 h in 5% milk in PBST (137 mM NaCl, 2.7 mM KCl, 8 mM Na_2HPO_4, 2 mM KH_2PO_4, and 0.1% Tween). Membranes were subsequently probed for 1 h using a monoclonal Anti-FLAG-Peroxidase antibody (Millipore Sigma, #A8592) at a 1:5000 dilution in PBS-T containing

5% milk. After six 5-min washes in PBST, membranes were developed using the Amersham ECL western blotting detection reagent (GE Healthcare).

AlphaFold prediction

The AlphaFold Server (https://alphafoldserver.com/), powered by AlphaFold 3 (75), was used to predict the interaction between DbfQ and DbfS. The interaction interface was predicted between the secreted form of DbfQ (beginning at residue 32) and full-length DbfS, with an interface predicted template modeling (ipTM) score of 0.69. The highest-ranked prediction based on reported confidence scores was selected for further visualization and analysis. Structural figures illustrating the predicted protein complexes were prepared using PyMOL (Schrödinger, LLC).

Purification and pull-down assays for DbfQ and DbfS^{SD}

DNA encoding processed DbfQ-6xHis (residues 32 to 135, excluding the secretion signal), and DbfS^{SD}-6xHis (residues 43 to 171) were cloned into the pET-15b vector via Gibson assembly (NEB), followed by transformation into chemically competent *E. coli* BL21 (DE3) cells. For protein purification, cultures were grown in Terrific broth (Fisher BioReagents) supplemented with 100 µg/mL ampicillin at 37°C for 4 h with shaking until OD_{600} ~ 0.6 - 0.8 was achieved. Protein expression was induced with 1 mM IPTG, followed by incubation at 18°C for 16 hours with continuous shaking. The following morning, cells were harvested by centrifugation (5,000 x g, 20 min, 4°C) and resuspended in lysis buffer (25 mM Tris–HCl pH 7.5, 300 mM NaCl, 10 mM imidazole, 10% glycerol, 0.5 mg/mL lysozyme, 25 U/mL benzonase nuclease, and 1x EDTA-free protease inhibitor tablet (Thermo Scientific). To stimulate lysis, resuspended cells were subjected to sonication (4 minutes total; 30 seconds on, 1:30 off; 8x cycles). Lysates were then subjected to centrifugation (15,000 rpm, 20 min, 4°C). Supernatants were filtered through 0.45-µm filters (Cytiva, #4654) and loaded onto Ni-NTA resin (EMD Millipore, #70666-4) pre-equilibrated with lysis buffer. After lysate flow-through was completed, columns were washed 3 times with 10x column volumes of wash buffer (25 mM Tris–HCl pH 7.5, 300 mM NaCl, 10 mM imidazole, 10% glycerol), after which bound proteins were eluted with elution buffer (25 mM Tris–HCl pH 7.5, 100 mM NaCl, 300 mM imidazole, 10% glycerol). The 6xHis tag on DbfQ was removed by thrombin cleavage (Cytiva Thrombin Protease, #45001320), and cleaved DbfQ was separated from the His-tag and uncleaved protein by repeated Ni-NTA affinity chromatography. Proteins were then dialyzed into storage buffer (25 mM Tris–HCl pH 7.5, 100 mM NaCl) using 3,500 molecular weight cut-off dialysis cassettes (Thermo Scientific, #66330) overnight at 4°C. Protein purity and concentration were assessed by SDS-PAGE and Pierce BCA Protein Assay (Thermo Scientific, #23225), respectively. Aliquots of proteins were flash-frozen in liquid nitrogen and stored at -80°C for subsequent use.

For pull-down assays, 50 µM of DbfQ (6xHis tag-cleaved) and 50 µM of DbfS^{SD}-6xHis were mixed in binding buffer (25 mM Tris–HCl pH 7.5, 100 mM NaCl, 1x EDTA-free protease inhibitor tablet). The protein mixture was incubated for 1 h at 25°C, then applied to Ni-NTA resin. After three washes with wash buffer, bound proteins were eluted with elution buffer and analyzed by SDS-PAGE. As controls, individual DbfQ (6xHis tag-cleaved) and DbfS^{SD}-6xHis were incubated with Ni-NTA resin under identical conditions.

Microscale thermophoresis (MST) analysis

Experiments were performed as described previously with minor modifications (76). Before labeling with fluorescent probes, DbfQ was diluted, and buffer exchanged into buffer M (20 mM MES, 100 mM NaCl, 10% glycerol) to remove incompatible buffer components. For protein labeling, 10 µM DbfQ was mixed with 3x excess Red NHS dye (Nanotemper Technologies) dissolved in DMSO and incubated at room temperature in the dark for 30 min. After incubation, excess and unreacted dye was removed by passing the protein-dye mixture through a gel-filtration column (Column B, Nanotemper Technologies). Optimal protein labeling was determined using the formula: A_{650}/195,000/M/cm x concentration of labeled protein; A_{650} = absorbance at 650 nm, and 195,000/M/cm is the molar absorbance of the Red NHS dye. An optimal labeling was considered as a value between 0.6 and 1.

For MST experiments, unlabeled DbfS protein was serially diluted in low binding tubes in buffer M supplemented with 0.05% Tween 20 at pH 7.5. The labeled DbfQ protein was added and incubated for 5 min at room temperature. The concentration of unlabeled DbfS ranged from 0.49 nM to 16,105 nM while the concentration of the labeled DbfQ was kept constant (20 nM). After incubation, samples were loaded into standard Monolith NT.115 capillary tubes and thermophoresis was determined using the Monolith MST device (Nanotemper Technologies) with the following parameters: 20%–60% excitation power and medium MST Power at 25°C. Thermophoresis results were analyzed using the PALMIST (77) and GUSSI (78) analysis pipeline. Briefly, data from Monolith Software were imported into the PALMIST software and a preset T-jump (TJ) was applied to the data using a 1:1 binding model with 95% confidence interval. After data analysis, figures were rendered using GUSSI. For stoichiometry determination, DbfQ-NHS (100 nM) was titrated against narrow increasing concentrations of unlabeled DbfS (0 nM to 40,000 nM) using 20%–60% excitation power and medium MST Power at 25°C. Fluorescence values were converted into relative thermophoresis by dividing the normalized fluorescence by the resulting amplitude at each data point.

RNA-sequencing

Cultures of the indicated *V. cholerae* strains, grown in triplicate, were diluted to OD_{600} ~0.001 in 5 mL of M9 medium. Subcultures were incubated at 30°C with shaking until OD_{600} 0.1 was reached. At this point, cells were collected by centrifugation for 10 min at 3,200x g and resuspended in RNAprotect (Qiagen). RNeasy mini kit (Qiagen) was used for RNA isolation and a TURBO DNA-free kit (Invitrogen) was used to remove remaining DNA. The concentration and purity of RNA were measured using a NanoDrop instrument (Thermo). Samples were frozen in liquid nitrogen and stored at −80°C until they were shipped on dry ice to the Microbial Genome Sequencing Center (now SeqCoast). Upon sample submission, the 12 million paired-end reads option and the intermediate analysis package were selected for each sample. As per the MIGS project report, quality control and adapter trimming were performed with bcl2fastq (Illumina), while read mapping was performed with HISAT2 (79). Read quantitation was performed using Subread's featureCounts (80) functionality, and subsequently, counts were loaded into R (R Core

Team) and normalized using edgeR's (81) Trimmed Mean of M values (TMM) algorithm. Values were converted to counts per million (cpm), and differential expression analyses were performed using edgeR's QuasiLinear F-Test (qlfTest) functionality against treatment groups, as indicated. Kegg pathway analysis was performed using limma's (56) *"kegga"* functionality with default parameters. Genes considered Up/Down in this analysis had a false discovery rate < 0.05. Plots, including heatmaps, pathway regulation, and volcano plots were produced in RStudio using the ggplot2 package.

Motility assay

Motility assays were performed on 6-well plates containing 1% tryptone, 0.5% NaCl, and 0.3% agar. *V. cholerae* strains were first grown overnight on LB agar plates at 30°C. A single colony from each strain was picked by a sterile pipette tip and inoculated into the center of each well of the motility plates. Plates were incubated at 37°C for 16 h, during which images were taken every hour using an Epson V750 Pro flatbed scanner. Motility was quantified by measuring the diameter of the motility zone for each strain in ImageJ. All statistical analyses in this study were performed using GraphPad Prism version 10.4.1 (GraphPad Software, San Diego, CA, USA).

c-di-GMP reporter assay

The c-di-GMP reporter assays were performed as previously described (58) Strains were constructed by conjugation with *E.coli* Top10 and S17 cells. Briefly, overnight *V. cholerae* cultures were diluted 1:5000 into M9 medium supplemented with 15 µg/mL gentamicin and transferred into 96-well plates sealed with a breathe-easier membrane. Plates were incubated overnight at 37°C with shaking. The following day, membrane was removed, and reporter measurements were obtained using a Tecan Spark plate reader using AmCyan (ex: 430 ± 20 nm, em: 490± 20 nm) and Turbo RFP (ex: 520 ± 20 nm, em: 580 ± 20 nm) channels. Relative fluorescence intensity (RFI) was calculated as the c-di-GMP regulated TurboRFP signal divided by constitutive AmCyan signal, and RFI values of mutants were normalized to WT signal.

***In vitro* and *in vivo* competition assays**

Competition assays were conducted to assess fitness of mutant *V. cholerae* strains relative to a WT reference strain (*lacZ*−) both in LB medium (*in vitro*) and in an infant mouse model (*in vivo*). For both assays, bacterial cultures were grown aerobically for ~18 h in LB medium at 30°C. For *in vitro* assays, ~10^5 CFU of each competing strain were mixed 1:1 in LB medium containing glass beads (to disrupt biofilms, as has been done previously) and incubated for 24 h at 30 °C. At the onset of the experiment and after 24 h of competition, samples were collected, serially diluted, and plated on LB/X-gal plates to enumerate CFUs for each strain. For *in vivo* competition assays, competing strains were mixed equally at a 1:1 ratio, and approximately 10^6 CFU were administered orogastrically to 4- to 7-day-old CD-1 mice (Charles River Laboratories). Prior to infection, infant mice were housed with their dam with ample access to food and water for at least 24 h and monitored. Serial dilutions of the intestinal homogenates were plated on LB/X-gal agar plates, allowing for CFU enumeration. In both assays, competitive index (CI) was calculated as the ratio of output to input of the mutant strain relative to the WT. For *in vitro* assays, three biological replicates were performed, while a minimum of five mice were

used for each *in vivo* experiment. Each biological replicate (*in vitro*) or individual mouse (*in vivo*) was treated as a single data point, and results are presented as the median with interquartile range. All animal experiments were approved by the Institutional Animal Care and Use Committee at Tufts University School of Medicine (Protocol B2024-26).

Acknowledgements

We thank members of the Bridges lab for their insightful discussions and detailed feedback on the manuscript. We especially thank Dr. Bonnie Basler for guidance and for sharing strains. This work was supported by NIH grant R00AI158939, a Shurl and Kay Curci Foundation grant (https://curcifoundation.org/), a Kaufman Foundation New Investigator Research Grant KA2023-136488 (https://kaufman.pittsburghfoundation.org/), a Damon Runyon Cancer Research Foundation Dale F. Frey Award for Breakthrough Scientists 2302-17 (https://www.damonrunyon.org/), and startup funds from Carnegie Mellon University to AAB. WLN and AS were supported by NIH grant R01AI121337. LAC was supported by startup funds provided by the University of Pittsburgh. MRP was supported by the CMLH Fellowship for Digital Health Innovation. The funders had no role in study design, data collection and analysis, decision to publish, or manuscript preparation.

Data Availability Statement

The source data used to generate all main and supporting figures in this work are available on Figshare, or as Supplemental Datasets. Biological materials used in this study are available upon request from Carnegie Mellon University.

Ethics Statement

All animal experiments were done in accordance with NIH guidelines, the Animal Welfare Act, and US federal law. The infant mouse colonization experimental protocol B2024-26 was approved by Tufts University School of Medicine's Institutional Animal Care and Use Committee. All animals were housed in a centralized and AAALAC-accredited research animal facility that is fully staffed with trained husbandry, technical, and veterinary personnel in accordance with the regulations of the Comparative Medicine Services at Tufts University School of Medicine

References

1. R. Gao, A. M. Stock, Biological Insights from Structures of Two-Component Proteins. *Annu Rev Microbiol* **63**, 133–154 (2009).
2. F. Jacob-Dubuisson, A. Mechaly, J.-M. Betton, R. Antoine, Structural insights into the signalling mechanisms of two-component systems. *Nat Rev Microbiol* **16**, 585–593 (2018).
3. E. A. Groisman, Feedback Control of Two-Component Regulatory Systems. *Annu Rev Microbiol* **70**, 103–124 (2016).
4. A. Y. Mitrophanov, E. A. Groisman, Signal integration in bacterial two-component regulatory systems. *Genes Dev* **22**, 2601–2611 (2008).
5. A. M. Stock, V. L. Robinson, P. N. Goudreau, Two-Component Signal Transduction. *Annual Review of Biochemistry* **69**, 183–215 (2000).
6. X. Shi, *et al.*, Bioinformatics and experimental analysis of proteins of two-component systems in *Myxococcus xanthus*. *Journal of Bacteriology* **190**, 613–624 (2008).
7. D. E. Whitworth, P. J. A. Cock, Evolution of prokaryotic two-component systems: insights from comparative genomics. *Amino Acids* **37**, 459–466 (2009).
8. D. Kim, S. Forst, Genomic analysis of the histidine kinase family in bacteria and archaea. *Microbiology* **147**, 1197–1212 (2001).
9. M. Y. Galperin, Diversity of Structure and Function of Response Regulator Output Domains. *Curr Opin Microbiol* **13**, 150–159 (2010).
10. B. M. Prüß, Involvement of Two-Component Signaling on Bacterial Motility and Biofilm Development. *Journal of Bacteriology* **199**, 10.1128/jb.00259-17 (2017).
11. A. N. Norsworthy, K. L. Visick, Signaling between two interacting sensor kinases promotes biofilms and colonization by a bacterial symbiont. *Molecular Microbiology* **96**, 233–248 (2015).
12. J. F. Brooks, M. J. Mandel, The Histidine Kinase BinK Is a Negative Regulator of Biofilm Formation and Squid Colonization. *Journal of Bacteriology* **198**, 2596–2607 (2016).
13. J. E. Heindl, *et al.*, Reciprocal control of motility and biofilm formation by the PdhS2 two-component sensor kinase of *Agrobacterium tumefaciens*. *Microbiology* **165**, 146–162 (2019).
14. J. Yan, B. L. Bassler, Surviving as a Community: Antibiotic Tolerance and Persistence in Bacterial Biofilms. *Cell Host & Microbe* **26**, 15–21 (2019).
15. L. Vidakovic, *et al.*, Biofilm formation on human immune cells is a multicellular predation strategy of *Vibrio cholerae*. *Cell* **186**, 2690-2704.e20 (2023).
16. C. Matz, *et al.*, Biofilm formation and phenotypic variation enhance predation-driven persistence of *Vibrio cholerae*. *Proc Natl Acad Sci U S A* **102**, 16819–16824 (2005).
17. R. M. Donlan, J. W. Costerton, Biofilms: Survival Mechanisms of Clinically Relevant Microorganisms. *Clin Microbiol Rev* **15**, 167–193 (2002).
18. C. D. Nadell, B. L. Bassler, A fitness trade-off between local competition and dispersal in *Vibrio cholerae* biofilms. *Proceedings of the National Academy of Sciences* **108**, 14181–14185 (2011).

19. P. G. Jayathilake, *et al.*, Extracellular Polymeric Substance Production and Aggregated Bacteria Colonization Influence the Competition of Microbes in Biofilms. *Front. Microbiol.* **8** (2017).
20. L. A. Meirelles, *et al.*, *Pseudomonas aeruginosa* faces a fitness trade-off between mucosal colonization and antibiotic tolerance during airway infection. *Nat Microbiol* **9**, 3284–3303 (2024).
21. K. Sauer, *et al.*, The biofilm life cycle: expanding the conceptual model of biofilm formation. *Nat Rev Microbiol* **20**, 608–620 (2022).
22. C. Guilhen, C. Forestier, D. Balestrino, Biofilm dispersal: multiple elaborate strategies for dissemination of bacteria with unique properties. *Molecular Microbiology* **105**, 188–210 (2017).
23. J. K. Teschler, C. D. Nadell, K. Drescher, F. H. Yildiz, Mechanisms Underlying *Vibrio cholerae* Biofilm Formation and Dispersion. *Annu. Rev. Microbiol.* **76**, 503–532 (2022).
24. C. Lutz, M. Erken, P. Noorian, S. Sun, D. McDougald, Environmental reservoirs and mechanisms of persistence of *Vibrio cholerae*. *Front Microbiol* **4**, 375 (2013).
25. R. Tamayo, B. Patimalla, A. Camilli, Growth in a Biofilm Induces a Hyperinfectious Phenotype in *Vibrio cholerae*. *Infect Immun* **78**, 3560–3569 (2010).
26. A. L. Gallego-Hernandez, *et al.*, Upregulation of virulence genes promotes *Vibrio cholerae* biofilm hyperinfectivity. *Proceedings of the National Academy of Sciences* **117**, 11010–11017 (2020).
27. D. Beier, R. Gross, Regulation of bacterial virulence by two-component systems. *Curr Opin Microbiol* **9**, 143–152 (2006).
28. E. Calva, R. Oropeza, Two-component signal transduction systems, environmental signals, and virulence. *Microb Ecol* **51**, 166–176 (2006).
29. Y. Liu, *et al.*, *Vibrio cholerae* senses human enteric α-defensin 5 through a CarSR two-component system to promote bacterial pathogenicity. *Commun Biol* **5**, 1–11 (2022).
30. A. A. Bridges, C. Fei, B. L. Bassler, Identification of signaling pathways, matrix-digestion enzymes, and motility components controlling *Vibrio cholerae* biofilm dispersal. *Proceedings of the National Academy of Sciences* **117**, 32639–32647 (2020).
31. P. D. Karp, *et al.*, The BioCyc collection of microbial genomes and metabolic pathways. *Brief Bioinform* **20**, 1085–1093 (2019).
32. F. Teufel, *et al.*, SignalP 6.0 predicts all five types of signal peptides using protein language models. *Nat Biotechnol* **40**, 1023–1025 (2022).
33. J. Mistry, *et al.*, Pfam: The protein families database in 2021. *Nucleic Acids Research* **49**, D412–D419 (2021).
34. N. Gallois, *et al.*, Discovery and characterization of UipA, a uranium- and iron-binding PepSY protein involved in uranium tolerance by soil bacteria. *ISME J* **16**, 705–716 (2022).
35. C. Yeats, N. D. Rawlings, A. Bateman, The PepSY domain: a regulator of peptidase activity in the microbial environment? *Trends in Biochemical Sciences* **29**, 169–172 (2004).
36. E. J. Capra, M. T. Laub, The Evolution of Two-Component Signal Transduction Systems. *Annu Rev Microbiol* **66**, 325–347 (2012).

37. Y. M. Zalucki, M. P. Jennings, Signal peptidase I processed secretory signal sequences: Selection for and against specific amino acids at the second position of mature protein. *Biochemical and Biophysical Research Communications* **483**, 972–977 (2017).
38. J. E. Musik, Y. M. Zalucki, C. J. Day, M. P. Jennings, Efficient function of signal peptidase 1 of *Escherichia coli* is partly determined by residues in the mature N-terminus of exported proteins. *Biochimica et Biophysica Acta (BBA) - Biomembranes* **1861**, 1018–1022 (2019).
39. J. E. Musik, *et al.*, New Perspectives on *Escherichia coli* Signal Peptidase I Substrate Specificity: Investigating Why the TasA Cleavage Site Is Incompatible with LepB Cleavage. *Microbiology Spectrum* **11**, e05005 (2023).
40. M. Jerabek-Willemsen, *et al.*, MicroScale Thermophoresis: Interaction analysis and beyond. *Journal of Molecular Structure* **1077**, 101–113 (2014).
41. Z. N. Freeman, S. Dorus, N. R. Waterfield, The KdpD/KdpE Two-Component System: Integrating K+ Homeostasis and Virulence. *PLOS Pathogens* **9**, e1003201 (2013).
42. E. A. Groisman, A. Duprey, J. Choi, How the PhoP/PhoQ System Controls Virulence and Mg2+ Homeostasis: Lessons in Signal Transduction, Pathogenesis, Physiology, and Evolution. *Microbiology and Molecular Biology Reviews* **85**, 10.1128/mmbr.00176-20 (2021).
43. C. Shaw, M. Hess, B. C. Weimer, Two-component systems regulate bacterial virulence in response to the host gastrointestinal environment and metabolic cues. *Virulence* **13**, 1666–1680 (2022).
44. W.-L. Ng, *et al.*, Signal production and detection specificity in *Vibrio* CqsA/CqsS quorum-sensing systems. *Mol Microbiol* **79**, 1407–1417 (2011).
45. M. B. Neiditch, M. J. Federle, S. T. Miller, B. L. Bassler, F. M. Hughson, Regulation of LuxPQ Receptor Activity by the Quorum-Sensing Signal Autoinducer-2. *Molecular Cell* **18**, 507–518 (2005).
46. S. Hunke, R. Keller, V. S. Müller, Signal integration by the Cpx-envelope stress system. *FEMS Microbiology Letters* **326**, 12–22 (2012).
47. S. L. Kolar, *et al.*, NsaRS is a cell-envelope-stress-sensing two-component system of *Staphylococcus aureus*. *Microbiology (Reading)* **157**, 2206–2219 (2011).
48. N. N. K. Kreamer, J. C. Wilks, J. J. Marlow, M. L. Coleman, D. K. Newman, BqsR/BqsS Constitute a Two-Component System That Senses Extracellular Fe(II) in *Pseudomonas aeruginosa*. *J Bacteriol* **194**, 1195–1204 (2012).
49. G. Zhang, T. C. Meredith, D. Kahne, On the Essentiality of Lipopolysaccharide to Gram-Negative Bacteria. *Curr Opin Microbiol* **16**, 779–785 (2013).
50. R. F. Maldonado, I. Sá-Correia, M. A. Valvano, Lipopolysaccharide modification in Gram-negative bacteria during chronic infection. *FEMS Microbiology Reviews* **40**, 480–493 (2016).
51. B. W. Simpson, M. S. Trent, Pushing the envelope: LPS modifications and their consequences. *Nat Rev Microbiol* **17**, 403–416 (2019).
52. J. S. Matson, J. Livny, V. J. DiRita, A putative *Vibrio cholerae* two-component system controls a conserved periplasmic protein in response to the antimicrobial peptide polymyxin B. *PLoS One* **12**, e0186199 (2017).

53. J. Nesper, *et al.*, Comparative and Genetic Analyses of the Putative *Vibrio cholerae* Lipopolysaccharide Core Oligosaccharide Biosynthesis (*wav*) Gene Cluster. *Infect Immun* **70**, 2419–2433 (2002).
54. S. Schild, A.-K. Lamprecht, J. Reidl, Molecular and functional characterization of O antigen transfer in *Vibrio cholerae*. *J Biol Chem* **280**, 25936–25947 (2005).
55. A. Marchese, *et al.*, Antibacterial and antifungal activities of thymol: A brief review of the literature. *Food Chemistry* **210**, 402–414 (2016).
56. M. E. Ritchie, *et al.*, *limma* powers differential expression analyses for RNA-sequencing and microarray studies. *Nucleic Acids Research* **43**, e47 (2015).
57. C. M. Waters, W. Lu, J. D. Rabinowitz, B. L. Bassler, Quorum Sensing Controls Biofilm Formation in *Vibrio cholerae* through Modulation of Cyclic Di-GMP Levels and Repression of vpsT. *Journal of Bacteriology* **190**, 2527–2536 (2008).
58. A. A. Bridges, B. L. Bassler, Inverse regulation of *Vibrio cholerae* biofilm dispersal by polyamine signals. *eLife* **10**, e65487 (2021).
59. H. Zhou, *et al.*, Characterization of a natural triple-tandem c-di-GMP riboswitch and application of the riboswitch-based dual-fluorescence reporter. *Sci Rep* **6**, 20871 (2016).
60. M. Valentini, A. Filloux, Biofilms and Cyclic di-GMP (c-di-GMP) Signaling: Lessons from *Pseudomonas aeruginosa* and Other Bacteria. *J Biol Chem* **291**, 12547–12555 (2016).
61. J. G. Conner, D. Zamorano-Sánchez, J. H. Park, H. Sondermann, F. H. Yildiz, The ins and outs of cyclic di-GMP signaling in *Vibrio cholerae*. *Current Opinion in Microbiology* **36**, 20–29 (2017).
62. X. Liu, S. Beyhan, B. Lim, R. G. Linington, F. H. Yildiz, Identification and Characterization of a Phosphodiesterase That Inversely Regulates Motility and Biofilm Formation in *Vibrio cholerae*. *Journal of Bacteriology* **192**, 4541–4552 (2010).
63. G. Kitts, *et al.*, The Rvv two-component regulatory system regulates biofilm formation and colonization in *Vibrio cholerae*. *PLoS Pathog* **19**, e1011415 (2023).
64. A. A. Bridges, B. L. Bassler, The intragenus and interspecies quorum-sensing autoinducers exert distinct control over *Vibrio cholerae* biofilm formation and dispersal. *PLOS Biology* **17**, e3000429 (2019).
65. A. B. Dalia, Natural Cotransformation and Multiplex Genome Editing by Natural Transformation (MuGENT) of *Vibrio cholerae*. *Methods Mol Biol* **1839**, 53–64 (2018).
66. A. B. Dalia, E. McDonough, A. Camilli, Multiplex genome editing by natural transformation. *Proceedings of the National Academy of Sciences* **111**, 8937–8942 (2014).
67. J. A. Prentice, S. Kasivisweswaran, R. van de Weerd, A. A. Bridges, Biofilm dispersal patterns revealed using far-red fluorogenic probes. *PLOS Biology* **22**, e3002928 (2024).
68. Posit team, RStudio: Integrated Development Environment for R. (2024). Deposited 2024.
69. H. Wickham, *ggplot2: Elegant Graphics for Data Analysis* (Springer-Verlag New York, 2016).

70. T. Paysan-Lafosse, *et al.*, InterPro in 2022. *Nucleic Acids Research* **51**, D418–D427 (2023).
71. D. Szklarczyk, *et al.*, The STRING database in 2023: protein–protein association networks and functional enrichment analyses for any sequenced genome of interest. *Nucleic Acids Res* **51**, D638–D646 (2022).
72. C. K. Saha, R. Sanches Pires, H. Brolin, M. Delannoy, G. C. Atkinson, FlaGs and webFlaGs: discovering novel biology through the analysis of gene neighbourhood conservation. *Bioinformatics* **37**, 1312–1314 (2020).
73. M. K. Winson, *et al.*, Engineering the *luxCDABE* genes from *Photorhabdus* luminescens to provide a bioluminescent reporter for constitutive and promoter probe plasmids and mini-Tn5 constructs. *FEMS Microbiology Letters* **163**, 193–202 (1998).
74. J. T. Saavedra, J. A. Schwartzman, M. S. Gilmore, Mapping Transposon Insertions in Bacterial Genomes by Arbitrarily Primed PCR. *Curr Protoc Mol Biol* **118**, 15.15.1-15.15.15 (2017).
75. J. Abramson, *et al.*, Accurate structure prediction of biomolecular interactions with AlphaFold 3. *Nature* **630**, 493–500 (2024).
76. C. Agbavor, *et al.*, The chaperone PrsA2 regulates the secretion, stability, and folding of listeriolysin O during *Listeria monocytogenes* infection. *mBio* **15**, e00743-24 (2024).
77. T. H. Scheuermann, S. B. Padrick, K. H. Gardner, C. A. Brautigam, On the acquisition and analysis of microscale thermophoresis data. *Anal Biochem* **496**, 79–93 (2016).
78. C. A. Brautigam, Calculations and Publication-Quality Illustrations for Analytical Ultracentrifugation Data. *Methods Enzymol* **562**, 109–133 (2015).
79. D. Kim, J. M. Paggi, C. Park, C. Bennett, S. L. Salzberg, Graph-based genome alignment and genotyping with HISAT2 and HISAT-genotype. *Nat Biotechnol* **37**, 907–915 (2019).
80. Y. Liao, G. K. Smyth, W. Shi, featureCounts: an efficient general purpose program for assigning sequence reads to genomic features. *Bioinformatics* **30**, 923–930 (2014).
81. M. D. Robinson, D. J. McCarthy, G. K. Smyth, edgeR: a Bioconductor package for differential expression analysis of digital gene expression data. *Bioinformatics* **26**, 139–140 (2010).

Supplemental Figures

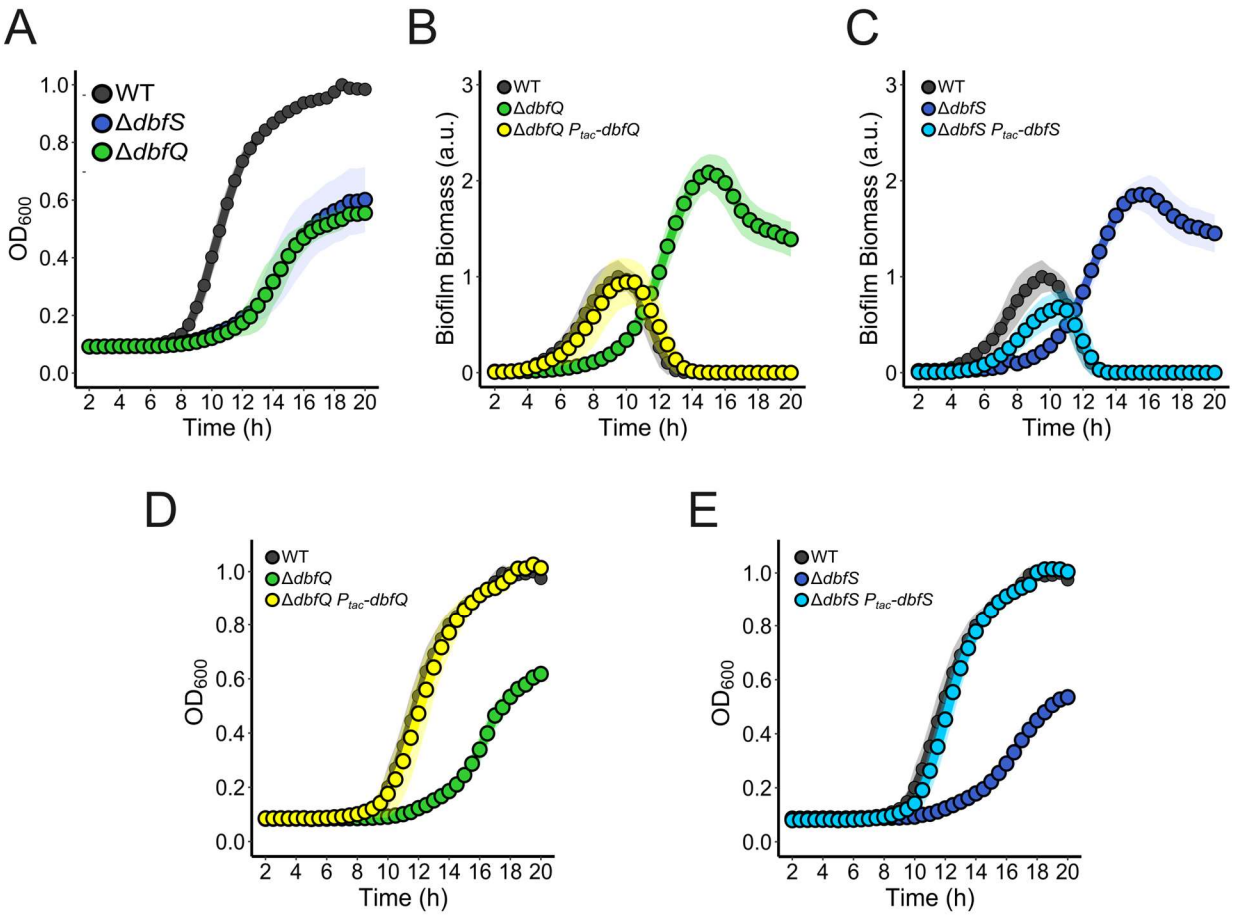

Figure S1: Δ*dbfQ* and Δ*dbfS* growth curves and complementation. (A) Growth curves of WT *V. cholerae* compared to the Δ*dbfQ* and Δ*dbfS* mutant strains as measured by OD_{600}. (B) Quantification of biofilm biomass over time using time-lapse brightfield microscopy for WT, Δ*dbfQ*, and Δ*dbfQ* P_{tac}-*dbfQ* expressed from an ectopic locus (*vc_1807*). (C) As in B for WT, Δ*dbfS*, and the Δ*dbfS* P_{tac}-*dbfS* complemented strain. (D) As in A for WT, Δ*dbfQ*, and Δ*dbfQ* P_{tac}-*dbfQ* complemented strain. (E) For all panels, points represent averages of $N = 2$ biological replicates and 3 technical replicates, ± SD (shaded regions).

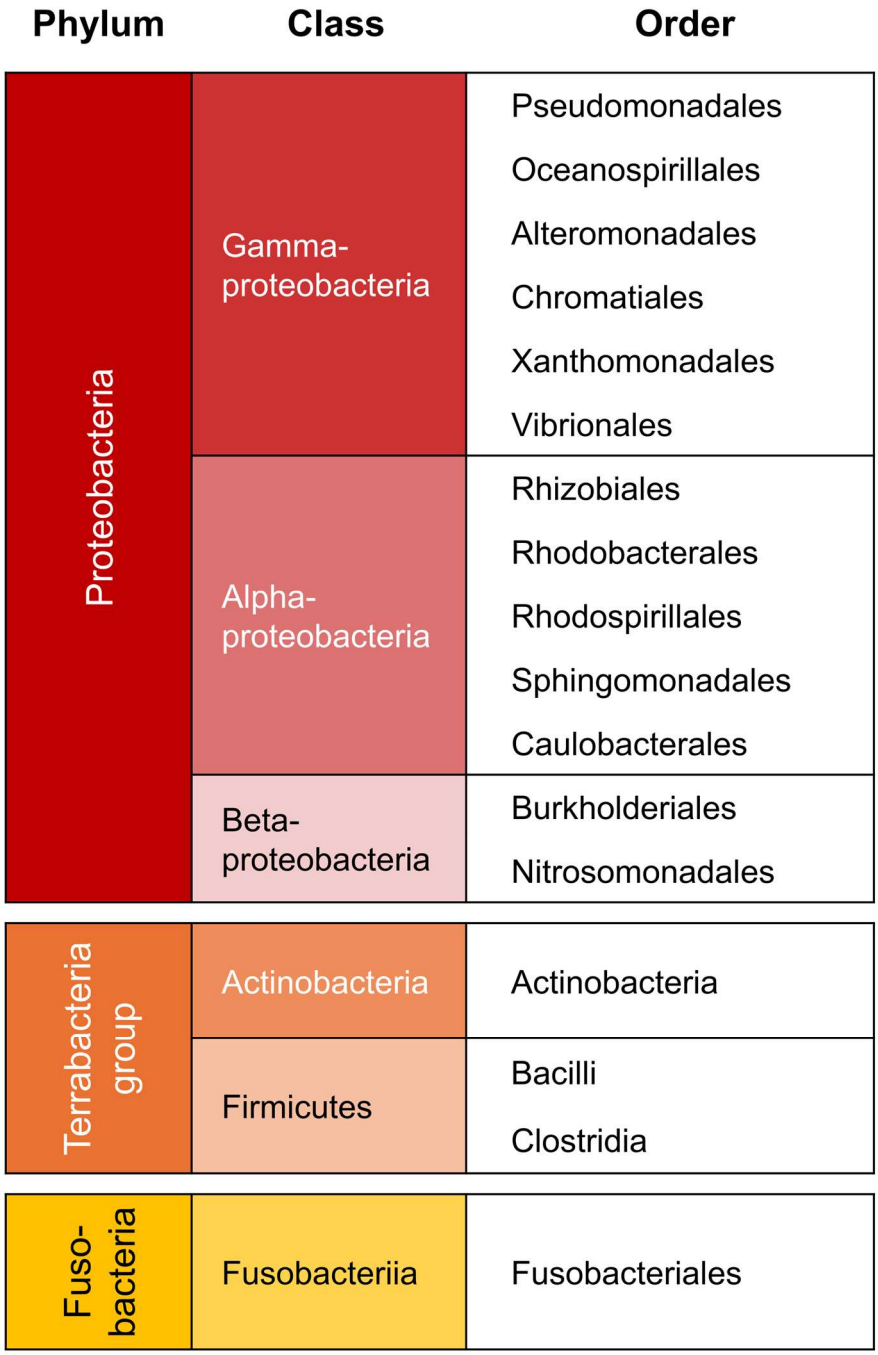

Figure S2: **Representative taxa encoding a PepSY domain-containing protein and a response regulator or histidine kinase within a 4-gene vicinity.** All taxa (phyla, classes and orders) that have a representation of 0.8% or higher are shown. Phyla are arranged from top to bottom by order of representation. A wide range of bacterial taxa encodes this module, with a large representation of γ-, α- and β-proteobacteria, actinobacteria, firmicutes, and a smaller representation of fusobacteria.

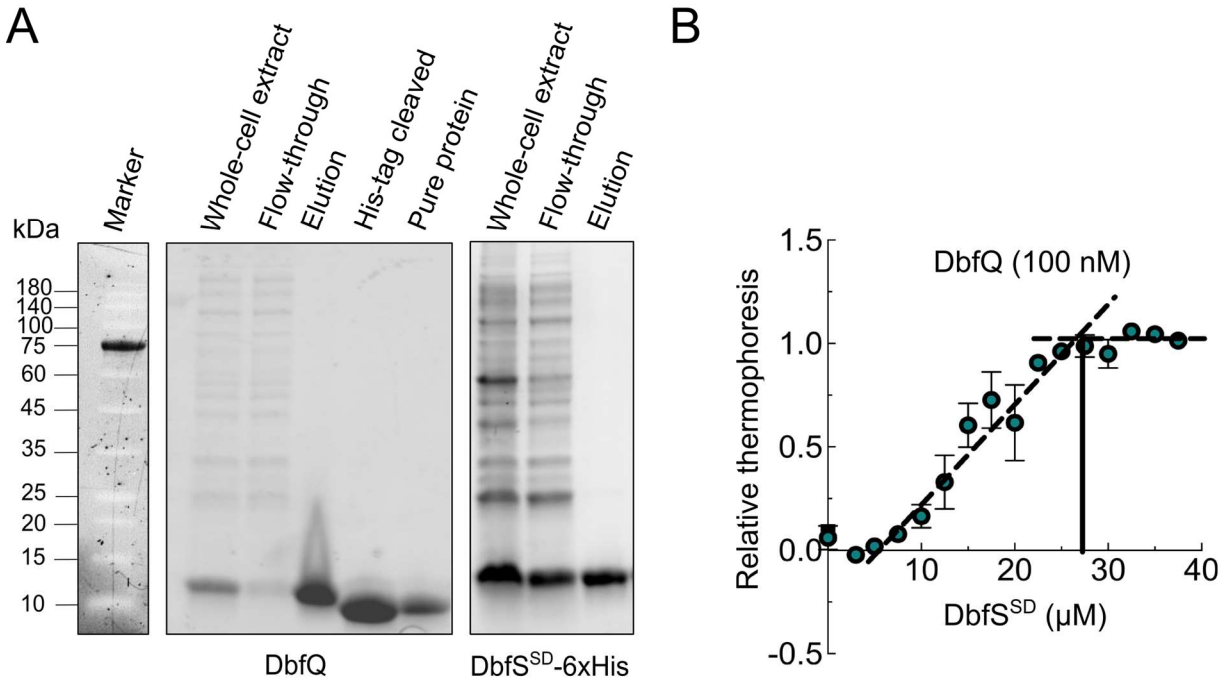

Figure S3: DbfQ and DbfS^{SD} purification and binding stoichiometry (A) Representative SDS-PAGE gel analyses of DbfQ-6xHis and DbfS^{SD}-6xHis protein purifications. The 6xHis tag of DbfQ was removed by thrombin cleavage for pull-down assays. (B) Microscale thermophoresis signals of labeled DbfQ titrated against narrow increasing concentrations of DbfS^{SD}. Dashed lines show the saturation point ("kink") of the data representing the occupancy of the DbfQ on its receptor, DbfS^{SD}, with an apparent binding ratio of 1:1. Data are presented as relative thermophoresis values ± SD of N = 4 independent measurements.

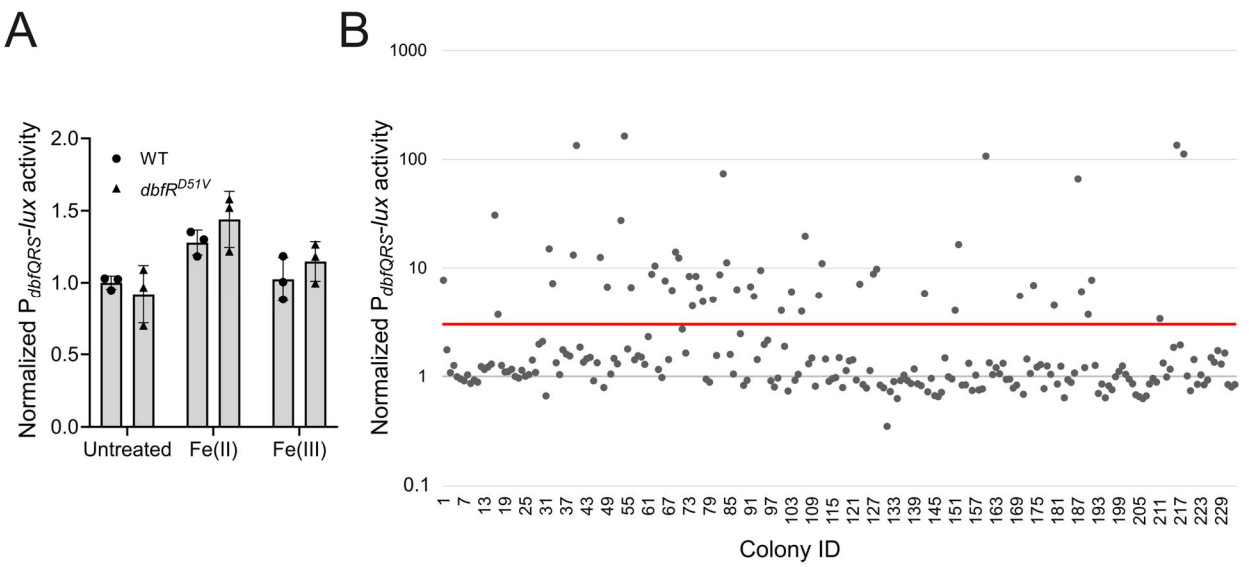

Figure S4: Identification of activators of the DbfQRS pathway. (A) P_{dbfQRS}-*lux* reporter activity in WT and *dbfR*^{D51V} strains measured in the presence of 100 µM Fe(II) or Fe(III). Data are presented as mean ± SD of peak RLU normalized to the average peak value of WT. Points represent individual replicates of 3 biological replicates. (B) Transposon mutagenesis screen for P_{dbfQRS}-*lux* reporter activation**.** Visual screening of ~20,000 colonies yielded 232 colonies with elevated luminescence compared to the parent strain. Luminescence outputs (relative light units, RLU) for these strains were subsequently quantified using a Biotek Cytation1 plate reader and normalized to the WT parental strain (normalized RLU = 1). The scatter plot shows the normalized RLU values for all 232 colonies, with a red solid line indicating a three-fold increase in RLUs. A total of 54 colonies exceeding this threshold were selected for transposon insertion site sequencing.

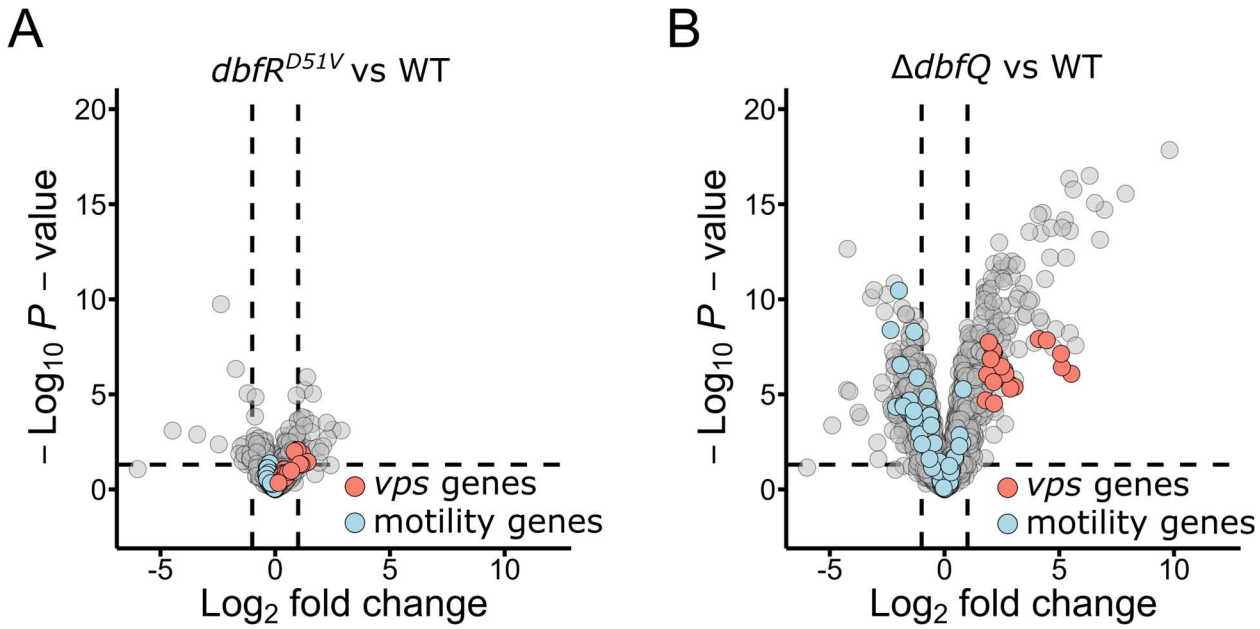

Figure S5: RNA sequencing results for *dbfR*^{D51V} and Δ*dbfQ* strains. (A) Volcano plot comparing fold changes and P-values for gene expression in the *dbfR*^{D51V} *V. cholerae* strain compared to WT. *vps* and motility genes are colored in orange and blue, respectively. The horizontal dotted line represents a -Log_{10} P-value of 0.05 and left and right vertical dashed lines represent Log_2 fold changes of −1 and 1, respectively. Samples were collected at OD_{600} = 0.1 and *N* = 3 biological replicates for each strain. Complete datasets are available in Dataset S1. (B) As in A, for the Δ*dbfQ* strain compared to WT. Complete datasets are available in Dataset S3.

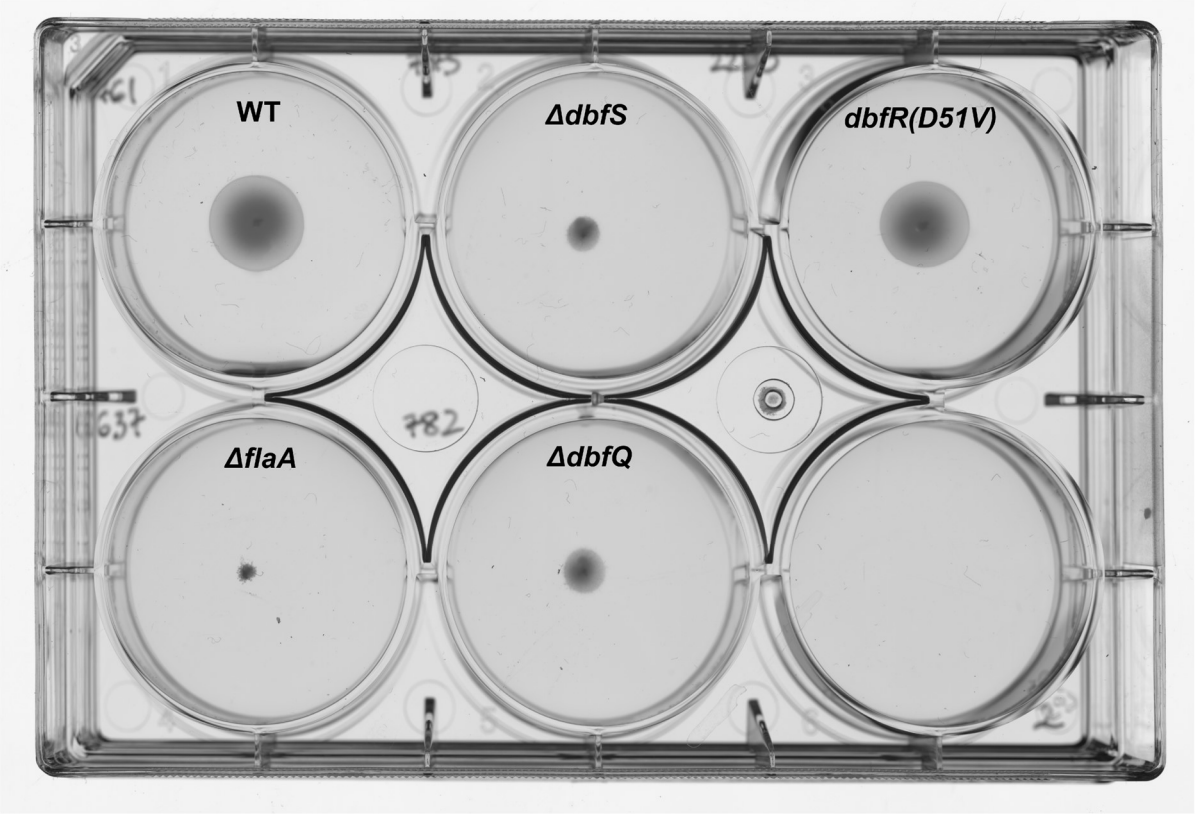

Figure S6: Motility assay for *V. cholerae* strains on soft agar plate (LB media, 0.3% agar). Representative image was captured after 10 hours of growth at 37° C. Results are representative of those from *N* = 6 biological replicates.

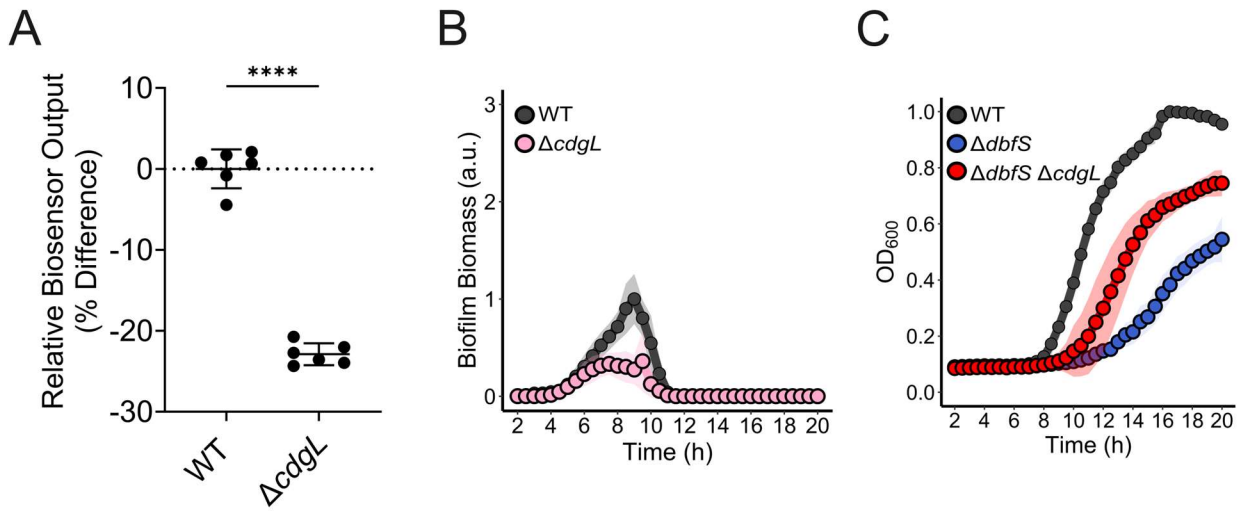

Figure S7: Deletion of *cdgL* decreases intracellular c-di-GMP levels and peak biofilm biomass compared to the WT *V. cholerae* strain. (A) Relative c-di-GMP reporter output for the WT and Δ*cdgL* strains, expressed as mean ± SD of the percentage difference relative to the WT control. Points represent individual replicates of $N = 2$ biological replicates and 3 technical replicates. Statistical analysis was performed using an unpaired, two-sample t-test (****, $P < 0.0001$). (B) Quantification of biofilm biomass for WT and Δ*cdgL* strains using time-lapse brightfield microscopy. Points represent averages of $N = 2$ biological replicates and 3 technical replicates, ± SD (shaded regions).

Table S1. List of transposon mutagenized genes resulting in elevated P_{dbfQRS}-*lux* activity.

Gene	Predicted Function	Times hit
LPS biosynthesis		
wavA (*vc_0223*)	HepIII transferase	2
wavB (*vc_0224*)	β1,4-glucosyl transferase	1
waaC (*vc_0225*)	HepI transferase	2
wavJ (*vc_0235*)	HepIV transferase	1
waaL (*vc_0237*)	O-antigen ligase	7
wavK (*vc_0238*)	O-acetyltransferase	6
wavL (*vc_0239*)	Glycosyltransferase	11
gmhD (*vc_0240*)	ADP-L-glycero-D-mannoheptose-6-epimerase	3
Transcription, Translation, and DNA repair		
vc_r004	16S ribosomal RNA	1
vc_r023	23S ribosomal RNA	2
vc_1130	DNA-binding protein H-NS	1
vc_1392	Deoxyribodipyrimidine photolyase	1
vc_1640	Ribosomal protein L25	1
vc_2030	Ribonuclease E	1
Transport		
lysW (*vc_1131*)	Na+/H+ antiporter NhaC family protein	1
epsL (*vc_2725*)	Type II secretion system protein L	1
Signal transduction		
dbfQ (*vc_1637*)	PepSY domain-containing protein	2
dbfS (*vc_1639*)	Histidine kinase	4
Metabolism		
vc_0550	Oxaloacetate decarboxylase	1
Hypothetical proteins		
vc_a0092		1
vc_0180		1
Phage shock protein		
pspA (*vc_1678*)	Phage shock protein A	2
Virulence		
rtxA (*vc_1451*)	RTX toxin RtxA	1
Total		**54**

1057

1058 **Table S2**: Gene disruptions identified as suppressing Δ*dbfS* colony rugosity.
1059
1060

Gene	Common Name	Hit Frequency
vc_0917	*vpsA*	14
vc_0916	*vpsU*	12
vc_0922	*vpsF*	12
vc_0665	*vpsR*	10
vc_0935	*vpsM*	10
vc_2285	*cdgL*	10
vc_0921	*vpsE*	9
vc_0925	*vpsI*	9
vc_0923	*vpsG*	8
vc_0924	*vpsH*	8
vc_0937	*vpsO*	8
vc_0934	*vpsL*	7
vc_2529	*rpoN*	7
vc_0920	*vpsD*	6
vc_0926	*vpsJ*	6
vc_0927	*vpsK*	6
vc_a0952	*vpsT*	6
vc_0395	*galU*	4
vc_0918	*vpsB*	4
vc_0919	*vpsC*	4
vc_0237	-	3
vc_0239	-	3
vc_a0774	*galE*	3
vc_1021	*luxO*	2
vc_0601	-	1
vc_0628	-	1
vc_0633	*ompU*	1
vc_0664	*lysS*	1
vc_0928	*rbmA*	1
vc_0932	*rbmE*	1
vc_0936	*vpsN*	1
vc_1609	-	1
vc_2423	*pilA*	1
vc_a0824	*ectB*	1
vc_0901	-	1

Table S3: Strains used in this study

Strain number	Genotype	Plasmid	Antibiotic resistance	Origin
AB_Vc_707	*Vibrio cholerae* C6706str2			Bassler lab
AB_Vc_761	Δ*vc1807*::Cm^R		Cm	NT of AB_Vc_707
AB_Vc_775	Δ*dbfS* Δ*vc1807*::Cm^R		Cm	NT of AB_Vc_707
AB_Vc_782	Δ*dbfQ* Δ*vc1807*::Cm^R		Cm	NT of AB_Vc_707
AB_Vc_788	*dbfR*^{D51V} Δ*vc1807*::Kan^R		Kan	NT of AB_Vc_707
AB_Vc_891	Δ*dbfS dbfR*^{D51V} Δ*vc1807*::Kan^R		Kan	NT of AB_Vc_707
AB_Vc_950	Δ*dbfQ dbfR*^{D51V} Δ*vc1807*::Kan^R		Kan	NT of AB_Vc_707
EN_Vc_2249	Δ*dbfQ* Δ*vc1807*::P$_{tac}$-*dbfQ*-Kan^R		Kan	NT of AB_Vc_707
EN_Vc_2261	Δ*dbfS* Δ*vc1807*::P$_{tac}$-*dbfS*-Spec^R		Spec	NT of AB_Vc_707
AB_Vc_863	*dbfR-SNAP* Δ*dbfS* Δ*vc1807*::P$_{BAD}$-*dbfS*::Spec^R		Spec	NT of AB_Vc_707
AB_Vc_964	*dbfR-SNAP* Δ*dbfQ* Δ*dbfS* Δ*vc1807*::P$_{BAD}$-*dbfS*::Spec^R		Spec	NT of AB_Vc_707
AB_Vc_1017	Δ*vc1807*::P$_{dbfQRS}$-*lux*::Spec^R		Spec	NT of AB_Vc_707
AB_Vc_1018	Δ*vpsL*::Cm^R Δ*vc1807*::*P$_{dbfQRS}$-lux*::Spec^R		Cm, Spec	NT of AB_Vc_707
AB_Vc_1020	Δ*dbfS* Δ*vpsL*::Cm^R Δ*vc1807*::P$_{dbfQRS}$-*lux*::Spec^R		Cm, Spec	NT of AB_Vc_707
AB_Vc_1030	*dbfR*^{D51V} Δ*vpsL*::Cm^R Δ*vc1807*::P$_{dbfQRS}$-*lux*::Spec^R		Cm, Spec	NT of AB_Vc_788
AB_Vc_1038	Δ*dbfQ* Δ*vpsL*::Cm^R Δ*vc1807*::P$_{dbfQRS}$-*lux*::Spec^R		Cm, Spec	NT of AB_Vc_1016
AB_Vc_1032	Δ*dbfS dbfR*^{D51V} Δ*vpsL*::Cm^R Δ*vc1807*::P$_{dbfQRS}$-*lux*::Spec^R		Cm, Spec	NT of AB_Vc_891
AB_Vc_1034	Δ*dbfQ dbfR*^{D51V} Δ*vpsL*::Cm^R Δ*vc1807*::P$_{dbfQRS}$-*lux*::Spec^R		Cm, Spec	NT of AB_Vc_950
AB_Vc_1036	*dbfQ-3xFlag* Δ*vpsL*:: Cm^R Δ*vc1807*::P$_{dbfQRS}$-*lux*::Spec^R		Cm, Spec	NT of AB_Vc_968
AB_Vc_1040	*dbfQ*^{A31W}*-3xFLAG* Δ*vpsL*::Cm^R Δ*vc1807*::P$_{dbfQRS}$-*lux*::Spec^R		Cm, Spec	NT of AB_Vc_707
AB_Vc_1050	*dbfQ*^{A31Y}*-3xFLAG* Δ*vpsL*::Cm^R Δ*vc1807*::P$_{dbfQRS}$-*lux*::Spec^R		Cm, Spec	NT of AB_Vc_979
AB_Vc_1052	*dbfQ*$^{\Delta sec}$*-3xFLAG* Δ*vpsL*::Cm^R Δ*vc1807*::P$_{dbfQRS}$-*lux*::Spec^R		Cm, Spec	NT of AB_Vc_979
AB_Vc_1004	Δ*vc1807*::P$_{tac}$-*dbfQ-mNG*-Kan^R		Kan	NT of AB_Vc_707

AB_Vc_1006	Δ*vc1807*::P_{tac}-*dbfQ*$^{\Delta sec}$-*mNG*-Kan^R		Kan	NT of AB_Vc_707
AB_Ec_086	*E. coli* BL21 (DE3)	pET15B::*dbfS*^{SD}-6xHis::AmpR	Amp	Transformation of BL21
AB_Ec_087	*E. coli* BL21 (DE3)	pET15B::*dbfQ*-6xHis::AmpR	Amp	Transformation of BL21
EN_Vc_2045	Δ*wavA* Δ*lacIZ*::Kan^R Δ*vpsL*::Cm^R Δ*vc1807*::P_{dbfQRS}-*lux*::Spec^R		Cm, Spec, Kan	NT of AB_Vc_1018
EN_Vc_2051	Δ*wavA dbfR*^{D51V} Δ*lacIZ*::Kan^R Δ*vpsL*::Cm^R Δ*vc1807*::P_{dbfQRS}-*lux*::Spec^R		Cm, Spec, Kan	NT of AB_Vc_1018
AB_Vc_637	Δ*flaA* P_{tac}-*mKO 1807:*Kan^R		Kan	Bassler lab
AB_Vc_996	Δ*cdgL* Δ*vc1807*::Kan^R		Kan	NT of AB_Vc_707
AB_Vc_1010	Δ*dbfS* Δ*cdgL* Δ*vc1807*::Cm^R		Cm	NT of AB_Vc_996
AB_Vc_956	*Vibrio cholerae* C6706str2	pFY4357::Gm^R	Gm	Conj of AB_Vc_707
IMB_Vc_2151	Δ*dbfS* Δ*cdgL* Δ*vc1807*::Cm^R	pFY4357::Gm^R	Gm	Conj of AB_Vc_1010
IMB_Vc_2156	Δ*cdgL* Δ*vc1807*::Kan^R	pFY4357::Gm^R	Gm	Conj of AB_Vc_996
IMB_Vc_2158	Δ*dbfS* Δ*vc1807*::Cm^R	pFY4357::Gm^R	Gm	Conj of AB_Vc_775
EN_Vc_2227	Δ*lacZ* Δ*vc1807*::Cm^R		Cm	NT of AB_Vc_1018
EN_Vc_2220	*dbfR*^{D51V} Δ*vc1807*::Cm^R		Cm	NT of AB_Vc_788

NT = Natural Transformation

Conj = Conjugation

1064 **Table S4**: DNA oligonucleotides and gene fragments used in this study.

Oligo #	Name	Purpose	Direction	5' to 3' Sequence
533	*vc1639*_3000up	Cloning at *dbfS* locus	F	GCTTAGTGATCGCAGAGCTTGC
534	*vc1639*_3000down	Cloning at *dbfS* locus	R	GTGCACTGCATTATTGACTCGCTTAGC
535	*vc1639*_100up	Cloning at *dbfS* locus	F	CAAGATTTTGACCGCGATTCCAATAC
536	*vc1639*_100down	Cloning at *dbfS* locus	R	G*TAGA*GTTTCCAAACCTATAGGAG
626	*vc1639*_Real_B	Deleting *dbfS*	R	CAACTGAAAATCCGTTTTTGCACCGCATTTAATTGGCATGCAACTGATACCCAAG
627	*vc1639*_Real_C	Deleting *dbfS*	F	CTTGGGTATCAGTTGCATGCCAATTAAATGCGGTGCAAAAACGGATTTTCAGTTG
559	*vc1639*_2700up	Cloning at *dbfS* locus	F	CAATCGGTGGTGCGCAACTTATCTGAG
560	*vc1639*_2700down	Cloning at *dbfS* locus	R	GTTAATGACTTGGAGCAGAATTAAGTTAGCCGC
654	*vc1637*_3000up	Cloning at *dbfQ* locus	F	GACTCACTTGCCGCCTACCTGCAAC
661	*vc1637*_3000down	Cloning at *dbfQ* locus	R	GCTGAGCGGGTAGAAGATGTTAATCAC
655	*vc1637*_2700up	Cloning at *dbfQ* locus	F	CTTGGTTTATTTCCAGATTGAGGCCAC
660	*vc1637*_2700down	Cloning at *dbfQ* locus	R	GAAATATCCATGCCGATCAGGTTCGTC
656	*vc1637*_100up	Cloning at *dbfQ* locus	F	GACTAGGCAAACCCAAAGCAGACGTTC
659	*vc1637*_100down	Cloning at *dbfQ* locus	R	GAGTACGATGACGTCCCACTCTTC
657	*vc1637*_B	Deleting *dbfQ*	R	CAACTAATATTTTCATGGTCTGCTCGATACCTGAATGTTGAATCTGTTGCCGAG
658	*vc1637*_C	Deleting *dbfQ*	F	CTCGGCAACAGATTCAACATTCAGGTATCGAGCAGACCATGAAAATATTAGTTG
650	*dbfR_D51V*_B	Generating *dbfR*^{D51V}	R	CAATTTCGGTAGGCCGAGTACGAGTACGATGACGTCC
651	*dbfR_D51V*_C	Generating *dbfR*^{D51V}	F	GGACGTCATCGTACTCGTACTCGGCCTACCGAAATTG
687	*vc1637_3xFLAG*_R	Generating *dbfQ-3xFLAG*	R	CGGATCCCGTCCCTGAAAATACAGGTTTTCTTTTTTGATGGCACGAATCACATTACGCC
688	*vc1637_3xFLAG*_F	Generating *dbfQ-3xFLAG*	F	ATCGATTACAAGGATGACGATGACAAGTGATCGAGCAGACCATGAAAATATTAGTTGTTGAAG
740	*vc1637_3xFLAG_gblock*	Gblock for generating *dbfQ-3xFLAG*	-	CGGGCGTAATGTGATTCGTGCCATCAAAAAAGAAAACCTGTATTTTCAGGGACGGGATCCGAATTCGAGCTCCGTCGACAAGCTTGCGGCCGCACTCGAGGACTACAAAGACCATGACGGTGATTATAAAGATCATGATATCGATTACAAGGATGACGATG

				ACAAGTGATCGAGCAGACCATGAAAAT ATTAGTTGTTGAAGATG
920	*dbfQ_deltaSec*_B	Generating *dbfQ*$^{\Delta sec}$	R	GTTCCCAGTCTCGCACCTTGTTATCCA ATACCTGAATGTTGAATCTGTTGCCG
921	*dbfQ_deltaSec*_C	Generating *dbfQ*$^{\Delta sec}$	F	CGGCAACAGATTCAACATTCAGGTATT GGATAACAAGGTGCGAGACTGGGAAC
916	*dbfQ_A31W*_B	Generating *dbfQ*^{A31W}	R	GTTCCCAGTCTCGCACCTTGTTATCCC AGTGAGTGGGCAGTGCAAACCCTAG
917	*dbfQ_A31W*_C	Generating *dbfQ*^{A31W}	F	CTAGGGTTTGCACTGCCCACTCACTG GGATAACAAGGTGCGAGACTGGGAAC
918	*dbfQ_A31Y*_B	Generating *dbfQ*^{A31Y}	R	GTTCCCAGTCTCGCACCTTGTTATCAT AGTGAGTGGGCAGTGCAAACCCTAG
919	*dbfQ_A31Y*_C	Generating *dbfQ*^{A31Y}	F	CTAGGGTTTGCACTGCCCACTCACTAT GATAACAAGGTGCGAGACTGGGAAC
866	pET15B_*dbfQ*_F	*pET15b-dbfQ-6xHis*	F	GAAATAATTTTGTTTAACTTTAAGAAGG AGATATACCATGGATAACAAGGTGCGA GACTGGGAACAAG
867	pET15B_*dbfQ*_R	*pET15b-dbfQ-6xHis*	R	GGCACCAGGCCGCTACCACTGCTTCC TTTTTTGATGGCACGAATCACATTACGC C
868	pET15B_*dbfS_LBD*_F	*pET15b-dbfS*^{SD}*-6xHis*	F	GAAATAATTTTGTTTAACTTTAAGAAGG AGATATACCATGAATCTCATCCATCAAT ATTTGCTGGAAG
869	pET15B_*dbfS_LBD*_R	*pET15b-dbfS*^{SD}*-6xHis*	R	GGCACCAGGCCGCTACCACTGCTTCC CTCTTTGCTCACGCGCTGTAGCGTG
736	*dbfR*_SNAP_deltaS_Gblock	Gblock for generating *dbfR-SNAP* and simultaneously deleting *dbfS*	-	CGCGGTCTTGGGTATCAGTTGCATGC CAATTCAGGAAGCGGCTCAGGCAGCG GATCAGGAATGGATAAGGATTGTGAAA TGAAGAGAACAACTT*TAGA*TTCCCCAC TAGGTAAAT*TAGA*ATTATCCGGTTGCGA ACAAGGATTACATCGTATTATATTTTTAG GAAAAGGAACCAGTGCAGCAGACGCC G*TAGA*AGTACCAGCCCCCGCCGCAGT TTTAGGAGGACCAGAACCACTAATGCA AGCCACCGCTTGGTTAAACGCATATTT TCATCAACCAGAAGCCA*TAGA*AGAATT CCCAGTACCAGCCCTACACCACCCAG TATTTCAACAAGAATCATTTACGAGACA AGTATTATGGAAATTATTAAAAGTCGTC AAATTCGGAGAAGTTATCAGCTATAGTC ACCTAGCCGCTCTTGCCGGTAATCCAG CAGCCACTGCCGCAGTTAAAACCGCA TTATCAGGTAACCCAGTTCCCATATTAA TTCCATGCCA*TAGA*GTAGTACAAGGAG ATT*TAGA*CGTCGGCGGATATGAAGGAG GTTTAGCAGTTAAAGAATGGTTACTAG CACATGAAGGACA*TAGA*TTAGGTAAAC CAGGATTAGGTTAAATGCGGTGCAAAA ACGGATTTTCAGTTGC
734	*dbfR*_R	Generating *dbfR*-SNAP and deleting *dbfS*	R	TTGGCATGCAACTGATACCCAAGACCG CG
735	*dbfS*_down_F	Generating *dbfR*-SNAP and deleting *dbfS*	F	ATGCGGTGCAAAAACGGATTTTCAGTT GC

672	SNAP_UnivR	Generating *dbfR*-SNAP	R	TTAACCTAATCCTGGTTTACCTAATCTATGTCCTTCATGTGCTAGTAACC
718	*dbfR*_SNAP_E	Generating *dbfR*-SNAP	F	GACA*TAGA*TTAGGTAAACCAGGATTAGGTTAAGATGTGATCAAAACTGTGCGCGGTC
105	BBC1881	Cloning at *vc1807* locus	F	TTTAAAGGGGATCAGTGACCG
106	BBC1882	Cloning at *vc1807* locus	R	CAATTTTGCTTTTGGACCATCCC
270	*1807*_2700up	Cloning at *vc1807* locus	F	GGCCGGCACTTTGATTACAATC
271	*1807*_2700down	Cloning at *vc1807* locus	R	GTCTATATCAGAGCGCTTAAAGAGCG
229	*1807*_100up	Cloning at *vc1807* locus	F	CATTGGTACAGAAGGCGGGTAG
230	*1807*_100down	Cloning at *vc1807* locus	R	GGTAAAGTCGTAGGCTCTGTCGCTG
2113	*vc1807*:P_{tac}-*dbfQ*-KanR_Fw	Complementation of *dbfQ* deletion	F	CGGGCGTAATGTGATTCGTGCCATCAAAAAATAAATTCCGGGGATCCGTCGAC
2114	*vc1807*:*P_{tac}-dbfS*-SpecR_Fw	Complementation of *dbfS* deletion	F	CCTAGGAATTCAATTAGGAGGTAATTAAGCTTGGGTATCAGTTGCATGCCAATTAAATC
721	P_{BAD}_*1807*_Univ_B	Generating P_{BAD}-*dbfS*	R	CATTTCACACCTCCTGCAGGTAC
722	P_{BAD}-*dbfS-1807*_C	Generating P_{BAD}-*dbfS*	F	GTACCTGCAGGAGGTGTGAAATGGGTATCAGTTGCATGCCAATTAAATCTCG
723	P_{BAD}-*dbfS-1807*_D	Generating P_{BAD}-*dbfS*	R	GTCGACGGATCCCCGGAATTTAATGGGATTTGACGGCTTTGGCTG
872	*1807*_B_univ	Generating P_{dbfQRS}-*lux*	R	CCTTAGCTACCCGCCTTCTGTACCAATG
873	P_{dbfQ}_*1807*_C	Generating P_{dbfQRS}-*lux*	F	CATTGGTACAGAAGGCGGGTAGCTAAGGCGTCCACCCCTGTTTGTGATTG
874	P_{dbfQ}_*lux*_D	Generating P_{dbfQRS}-*lux*	R	GTTAATAATGAATGAAATTTTTTTAGTCATAGTCAATACCTGAATGTTGAATCTGTTGCC
875	*lux*_F_univ	Generating P_{dbfQRS}-*lux*	F	ATGACTAAAAAAATTTCATTCATTATTAACGGCCAGG
876	*lux*_mid_2700down	Generating P_{dbfQRS}-*lux*	R	CATATCTGTGCCGAATACGCGAAAG
877	*lux*_mid_3000down	Generating P_{dbfQRS}-*lux*	R	CAACTTAATATCATCGGTAGGCCAAATTGAG
512	P_{tac}_RBS_R	RBS used with P_{tac}	R	GCTTAATTACCTCCTAATTGAATTCCTAGGCCTG
886	P_{tac}_*dbfQ*_C	Generating P_{tac}-*dbfQ-mNG*	F	CCTAGGAATTCAATTAGGAGGTAATTAAGCTTGACTATGCAGATTTTTCGTATGCAGC
887	*1807_mNG*_D	Generating P_{tac}-*dbfQ-mNG*	R	GTCGACGGATCCCCGGAATTCACTTGTACAGCTCGTCCATGCCCATC
888	P_{tac}_*nosec_dbfQ*_C	Generating P_{tac}-*$dbfQ^{\Delta sec}$ - mNG*	F	GCCTAGGAATTCAATTAGGAGGTAATTAAGCATGGATAACAAGGTGCGAGACTGGGAACAAG
232	ABD123	Universal upstream AbR cassette	F	ATTCCGGGGATCCGTCGAC

233	ABD124	Universal downstream AbR cassette	R	TGTAGGCTGGAGCTGCTTC
1801	*vc0223*_3000up	Cloning at *wavA* locus	F	GTGCGGCAAGTTAGTATAATGCGC
1802	*vc0223*_B	Deleting *wavA*	R	GGGAGCCGCAGCTCCCTTTTTTAATGATGTGCTCGATAAGGTGTGAAATTTTGCG
1803	*vc0223*_C	Deleting *wavA*	F	CGCAAAATTTCACACCTTATCGAGCACATCATTAAAAAAGGGAGCTGCGGCTCCC
1804	*vc0223*_3000down	Cloning at *wavA* locus	R	GGAGGTAATGGACGGTGTAATAGGTC
1805	*vc0223*_2700up	Cloning at *wavA* locus	F	GGTAAGCGTCCTGCAGTTGGTAAC
1806	*vc0223*_2700down	Cloning at *wavA* locus	R	CGGTGTGGTTGACTTGCGCATC
1807	*vc0223*_100up	Cloning at *wavA* locus	F	GCGCGCTCAATCAAATCCAGATG
1808	*vc0223*_100down	Cloning at *wavA* locus	R	GCACTGCTCTCTGCACACTCTACC
878	*cdgL*_3000up	Cloning at *cdgL* locus	F	CGCCGATTACCTTCAATCTCAAGGTATC
879	*cdgL*_2700up	Cloning at *cdgL* locus	F	GTTCGTTACTCGCATATCATCGATCCAACTAC
880	*cdgL*_100up	Cloning at *cdgL* locus	F	GATCCCTCAACTAAAGAACTATCAAGTCTTCACCATC
881	*cdgL*_B	Deleting *cdgL*	R	CAAATTTCAAATGATGTATCGTTTAAAATATCACCATCGTCATAATAAACCTTTAC
882	*cdgL*_C	Deleting *cdgL*	F	GTAAAGGTTTATTATGACGATGGTGATATTTTAAACGATACATCATTTGAAATTTG
883	*cdgL*_100down	Cloning at *cdgL* locus	R	GATTGTGCCATTACGACGACTCACGATAC
884	*cdgL*_2700down	Cloning at *cdgL* locus	R	GTAGCGGGTGTAGATCTGCTGCGTTC
885	*cdgL*_3000down	Cloning at *cdgL* locus	R	GTGAGTTTCGCTCGAACCTGCATCG
107	*lacZ*_3000up	Cloning at *lacZ* locus	F	GAGCACAAGGAGGGTGATTGAACTGATTAG
108	*lacZ*_3000down	Cloning at *lacZ* locus	R	CGCCAAAGCGACATCCTGCTCAATTGC
307	*lacZ*_2700up	Cloning at *lacZ* locus	F	CGTGATTGGGAGGATGCGCTCAGTG
147	*lacZ*_2900down	Cloning at *lacZ* locus	R	GTTCCCTCTTCGGTTATCGACAGTTTG
2092	*lacZ*_deletion_R	Deleting *lacZ*	R	CAGGGTGCACACTTTGGCTCCACGAATCCCCTCAAGCCGAGGAGTAAAGAAGTCATTC
2093	*lacZ*_deletion_F	Deleting *lacZ*	F	GAATGACTTCTTTACTCCTCGGCTTGAGGGGATTCGTGGAGCCAAAGTGTGCACCCTG
519	Arbitrary Primer	Transposon localization	F	GGCCACGCGTCGACTAGTACNNNNNNNNNNAGAG
520	Tn5 specific Primer	Transposon localization	R	GAAGCCCTTAGAGCCTCTC

521	Arbitrary PCR cleanup	Transposon localization	F	AGGAACACTTAACGGCTGAC
522	Arbitrary PCR cleanup	Transposon localization	R	GGCCACGCGTCGACTAGTAC